Official Journal of CIOMP
elight.springeropen.com

REVIEW

Open Access

Next generation lanthanide doped nanoscintillators and photon converters

Lei Lei[1*], Yubin Wang[1], Andrey Kuzmin[2], Youjie Hua[1], Jingtao Zhao[1], Shiqing Xu[1*] and Paras N. Prasad[2*]

Abstract

Scintillators are of significance for the realization of indirect X-ray detection and X-ray excited optical luminescence (XEOL) imaging. However, commercial bulk scintillators not only require complex fabrication procedures, but also exhibit non-tunable XEOL wavelength and poor device processability. Moreover, thick crystals usually generate light scattering followed by evident signal crosstalk in a photodiode array. Lanthanide doped fluoride nanoscintillators (NSs) prepared with low-temperature wet-chemical method possess several advantages, such as low toxicity, cheap fabrication cost, convenient device processability and adjustable emission wavelengths from ultraviolet to visible and extending to second near infrared window. In addition, they exhibit X-ray excited long persistent luminescence (XEPL) making them suitable for broadening the scope of their applications. This review discusses and summarizes the XEOL and XEPL characteristics of lanthanide doped fluoride NSs. We discuss design strategies and nanostructures that allow manipulation of excitation dynamics in a core–shell geometry to simultaneously produce XEOL, XEPL, as well as photon upconversion and downshifting, enabling emission at multiple wavelengths with a varying time scale profile. The review ends with a discussion of the existing challenges for advancing this field, and presents our subjective insight into areas of further multidisciplinary opportunities.

1 Introduction

X-rays are electromagnetic waves with short wavelength and strong penetrability in physical matter including live organisms [1–4]. Scintillators that are capable of converting X-rays into ultraviolet (UV), visible or near infrared (NIR) photons [5, 6], are widely employed to realize indirect X-ray detection and XEOL imaging in medical diagnosis [7, 8], computed tomography (CT) [9, 10], space exploration [11, 12] as well as in non-destructive industrial material [13, 14] and security inspections [15, 16]. Commercial bulk scintillators, such as $CaWO_4$ [17], NaI:Tl [18], $(Lu,Y)_2SiO_5$:Ce (LYSO:Ce) [19] and $Bi_4Ge_3O_{12}$ (BGO) [20], possess high light yield (LY) and superior energy resolution; however, they suffer from serval drawbacks, i.e., complex fabrication procedures, expensive experimental equipment, nontunable XEOL wavelength and poor device processability [21, 22]. Moreover, they all produce emission in the visible spectral range, but having XEOL in the NIR range may find more interesting applications in biomedicine [23, 24]. Also, thick crystals usually generate light scattering followed by evident signal crosstalk in a photodiode array [22, 25, 26]. Recently, metal halide perovskites, which can be prepared by facile low temperature or even by room-temperature approaches have been investigated for X-ray detection [27, 28]. Unfortunately, these materials exhibited some intrinsic limitations as well, such as poor photo-/environmental-stability, heavy metal toxicity and low LY [29–31]. Thus, the search for developing new generation of scintillators is still one of the topic of the day.

Lanthanide doped fluoride NSs not only avoid the above mentioned limitations of bulk scintillators and metal halide perovskites, but also exhibit many useful properties. By employing a cheap and convenient

*Correspondence: leilei@cjlu.edu.cn; shiqingxu@cjlu.edu.cn; pnprasad@buffalo.edu

[1] College of Optical and Electronic Technology, China Jiliang University, Hangzhou 310018, Zhejiang, China
[2] Institute for Lasers, Photonics, and Biophotonics and Department of Chemistry, University at Buffalo, The State University of New York, Buffalo, NY 14260, USA

© The Author(s) 2022. **Open Access** This article is licensed under a Creative Commons Attribution 4.0 International License, which permits use, sharing, adaptation, distribution and reproduction in any medium or format, as long as you give appropriate credit to the original author(s) and the source, provide a link to the Creative Commons licence, and indicate if changes were made. The images or other third party material in this article are included in the article's Creative Commons licence, unless indicated otherwise in a credit line to the material. If material is not included in the article's Creative Commons licence and your intended use is not permitted by statutory regulation or exceeds the permitted use, you will need to obtain permission directly from the copyright holder. To view a copy of this licence, visit http://creativecommons.org/licenses/by/4.0/.

wet-chemical method, the size, shape and core@shell structures of the lanthanide doped fluoride NSs can be tuned and designed on demand [32, 33]. Benefiting from the abundant energy levels of lanthanide activators, the emission wavelengths can be tuned from UV to visible and be extended to the second NIR window [34, 35]. Furthermore, these NSs show superior photostability [36–39], low toxicity [40, 41] and convenient device processability, which make them promising candidates for next generation NSs and in the emerging fields of XEOL imaging. Moreover, they exhibit XEPL property, which showing promising applications in biomedicine and optical information encoding [42, 43]. The combination of XEOL and XEPL making them suitable for broadening the scope of their applications [44]. In recent years, significant advances have been made in NS development, thus it is very timely to summarize present results for further enhancing their performances and expanding the applications.

In this review, we discuss the XEOL and XEPL characteristics of lanthanide doped fluoride NSs, which includes their mechanisms, tunable emission wavelengths from UV to visible then extending to second near infrared (NIR-II), performance indexes and optimization strategies as well as their corresponding applications. The emerging applications of NSs are summarized. We discuss design strategies and nanostructure that allow manipulation of excitation dynamics in a core–shell geometry that simultaneously produce XEOL, XEPL, as well as photon upconversion (UC) and downshifting (DS), enabling emission at multiple wavelengths and at varying time scales. A major feature of this review is summarizing the existing challenges in advancing this field, together with our subjective insight into areas of further multidisciplinary opportunities.

2 Fundamentals of scintillation

X-ray shows strong penetration ability even in dense matters [45, 46], which was first found by Wilhelm Roentgen in 1895 [47] and then broadly used in many fields [48, 49]. The hard X-ray (0.01–0.1 nm) is generally used for space exploration and non-destructive inspection of industrial equipment [11, 12], while the soft X-ray (0.1–10 nm) is widely employed in medical diagnosis and CT [9, 35]. Two types of X-ray detector are generally used to realize these practical applications; one is direct conversion of X-ray photons into electrical signals utilizing semiconductor materials (i.e., amorphous selenium) [50, 51]. The other one is indirect conversion into low-energy photons (i.e., ultraviolet and/or visible light) via scintillators, which are then detected by low cost arrayed photodetectors (i.e., amorphous Si photodiodes [52], photomultiplier tubes [53], silicon avalanche photodiode [54], charge-coupled devices [55], or complementary metal-oxide semiconductor [56]). Owing to rapid development of plentiful high-performance scintillators, cheap commercialized sensing arrays and flexible combinations, the indirect conversion route is becoming more popular for the detection of X-rays.

2.1 History and comparison of inorganic scintillators

Scintillators are the core component of an intact indirect X-ray detector device, which experienced more than hundred years of development [57–60]. Inorganic scintillators can be classified into intrinsic and extrinsic based on the XEOL mechanism [61, 62], or halides and oxides based on the anion type at present [63, 64]. The intrinsic XEOL mainly includes free-exciton luminescence (i.e., ZnO [65] and GaN [66]), self-trapped exciton (STE) luminescence (i.e., CaF_2 [67], SrF_2 [68] and BaF_2 [69]), Auger free luminescence (i.e., BaF_2 [69], $BaMgF_4$ [70], CsF [71] and Cs_2ZnCl_4 [72]) and self-activation luminescence (i.e., BGO [73], CeF_3 [74] and $CeBr_3$ [75]). The extrinsic XEOL originates from doped activators, i.e., Tl^+, Bi^{3+}, In^+, Sn^{2+}, Mn^{2+}, Cr^{3+} and lanthanide ions [76–79], or defects such as F-centers [80, 81], which offers the prospect to tune the emission wavelengths and improve the performance.

In the year 1895, Wilhelm Roentgen first reported that both barium platino-cyanide (Ba $[Pt(CN)_4]$) and calcium sulphide (CaS) emitted visible photons upon X-ray irradiation which could pass through 15 mm thick aluminum sheet [47]. Then $CaWO_4$ [82] and ZnS [83] were used as the first generation of scintillators. Because of the poor experimental conditions in this early stage, the occurrence of scintillation process was judged by the naked eye. During 1940s to 1960s, the second generation of scintillators, such as NaI (Tl) [84], CsI (Tl) [85], CaF_2 (Eu) [86] and $CdWO_4$ [87], was developed. CaF_2 and $CdWO_4$ are known as fluorite and scheelite in mineralogy, respectively [88]. After the development of BGO single crystal in 1973 [89], the Ce^{3+} activators incorporated third generation of scintillators were developed, i.e., Lu_2SiO_5: Ce (LSO: Ce) [90], LYSO: Ce [91] and $Gd_3(Al,Ga)_5O_{12}$: Ce (GAGG:Ce) [92]. Up to date, BaF_2, $CdWO_4$, BGO, Gd_2SiO_5: Ce (GSO: Ce), LSO: Ce, $LaBr_3$: Ce, GAGG: Ce, $Lu_3Al_5O_{12}$: Ce (LuAG: Ce), Gd_2O_2S: Tb bulk scintillators and thick CsI (Tl) films are widely commercialized [61, 93].

Each kind of scintillator has its own advantages and disadvantages, for example, the NaI (Tl) crystals exhibits high LY (38,000–68,000 photons/MeV) [94], but poor water stability and are fragile [95]; BaF_2 possesses ultra-fast decay rate [96], but low LY (10,400–11,800 photons/MeV) [97], are fragile and poor energy resolution [98]; GSO crystal shows higher LY than that of BGO and superior water stability [99], but requires expensive

fabrication procedures as well as poor energy resolution than that of CsI (Tl) [100]. Furthermore, these traditional scintillators suffer from several common drawbacks. First of all, these scintillators are generally prepared via complex and expensive fabrication procedures. For examples, LYSO:Ce is mainly synthesized by the Czochralski method at temperatures higher than 1500 °C [101] and LuAG:Ce is prepared by vacuum sintering ($<10^{-3}$ pa) at 1750 °C [102]. Secondly, these crystals are inherently brittle and fragile, which are difficult to be coupled with flexible detectors for XEOL imaging [103]. Thirdly, the XEOL wavelengths are mainly located in the visible range and hard to be tuned owing to the fixed electron transition processes [104]. Fourthly, the large thickness of these scintillators brings light scattering and then leads to evident signal crosstalk in a photodiode array [25, 26]. At last, radioluminescence afterglow can cause image artifacts and influence the high-contrast X-ray imaging quality, especially in CT and modern digital radiography [105, 106].

Recently, a large number of halide perovskites have been studied as a new class of scintillators. The high-Z ions, such as Cs, Pb, Bi and I, endow them large X-ray absorption coefficient and high LY up to 90,000 photons/MeV at 77 K [107]. In addition, their facile preparation processes make them easier to be formed as polycrystalline films, single crystals, and nanocrystals [22, 108]. Interested readers are referred to a few recent reviews covering the contents of synthesis, mechanism and performances [109]. Although great achievements have been made on these scintillators, their poor photo-/environmental- stability, high toxicity of heavy metal ions such as Pb, and low room temperature LY greatly restrict their practical applications. In addition, XEOL in these systems mainly originates from band gap transition, thus, the emission wavelengths usually remain limited to the visible range.

Lanthanide ions possess plentiful ladder-like energy levels and can produce emission wavelengths from UV, to visible, to NIR [110, 111]. Alkali or alkaline-earth fluoride nanoparticles are widely employed for the incorporation of lanthanide ions with high solubility up to 100%, exhibiting superior photostability (i.e., no photobleaching), stable emission capability (i.e., no blinking) and low toxicity [112–114]. Attributing to their mature and facile wet-chemical synthesis routes, such as co-precipitation, solvo-/hydro- thermal, and thermal decomposition, it is convenient to tune the particle size, shape, crystal phase, and chemical compositions, to modify the hydrophobic or hydrophilic surface, and to construct multifunctional core@shell nanoarchitectures [32, 33, 115]. Moreover, the high-Z lanthanide ions produce enhancement of X-ray absorption efficiency and therefore LY. For example, the LY of hexagonal $NaLuF_4$:Gd/Tb NSs was reported to be 39,460 ph/MeV [116]. These characteristics endow them next generation candidates for NSs and much suitable for the emerging fields of XEOL imaging and biomedicine, which will be discussed in the application section. Furthermore, the occurrence and tunability of XEPL make them suitable for broadening the scope of their applications. The history and comparison of common inorganic scintillators is shown in Fig. 1 [11, 86–88, 117–123].

2.2 Performance index of scintillator

X-ray absorption coefficient: The absorption coefficient (α) is the efficiency of a scintillator to absorb the incident X-ray photon energy in the conversion stage, which can be expressed by the following equation [1]:

$$\alpha = \rho Z^4/AE^3 \tag{1}$$

where ρ, Z, A and E are density, atomic number, atomic mass and radiation energy, respectively. The X-ray stopping power (also named as attenuation coefficient) of a scintillator with a given thickness mainly depends on α. Thus, the scintillators with high density and high-Z usually show better scintillation property and more suitable for X-ray detection [109]. For example, the absorption coefficient of $NaLuF_4$ (atomic number $Z_{max}=71$, $K\alpha=63.31$ keV) is larger than that of $NaYF_4$ ($Z_{max}=39$, $K\alpha=17.05$ keV), hence the XEOL and XEPL intensities of $NaLuF_4$:Tb NSs are stronger than that of $NaYF_4$:Tb NSs [44].

LY: LY is one of the most important performance indices for scintillators [124]. Absolute light yield refers to the ratio of total energy of scintillation photons to energy deposited by ionizing radiation in a scintillator, and can be characterized by the number of emitted photons per each 1 MeV radiation energy absorbed by a scintillator [125]. The number of emitted photons (N_{ph}) produced in scintillation can be calculated by the following equation [126]:

$$N_{ph} = \frac{E}{\beta E_g} \times SQ \tag{2}$$

where E (eV) is the energy of the incoming X-ray photon and E_g (eV) is the bandgap of the scintillator. S and Q are the quantum efficiencies in the transport and luminescence stages, respectively. β, indicating the average energy required to generate one thermalized electron–hole pair, is a phenomenological parameter which is typically found to be 2 ~ 3. Because a number of emitted photons might be lost before being captured by the photodetector, the actual light yield of a scintillator is always lower than the N_{ph} value.

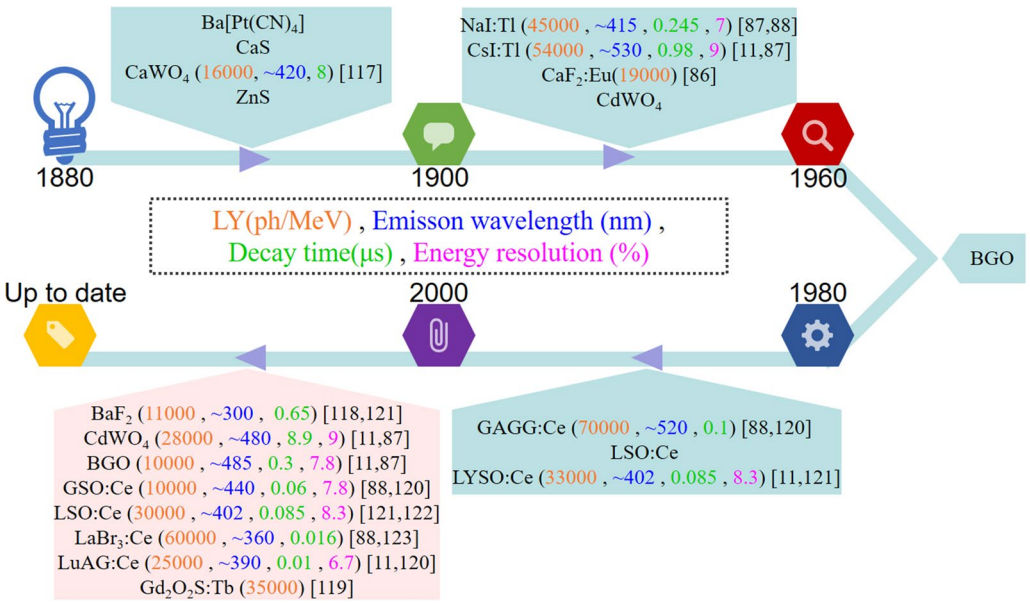

Fig. 1 History and comparison of common inorganic scintillators

Response—decay time: The response time represents how fast the scintillator converts X-ray photons to emitted photons such as UV or visible [109]. The decay rate of the luminescence center itself is defined by its transition dipole moment from the excited state to ground state. Introducing nonradiative quenching or energy transfer processes away from the excited state can accelerate the decay rate, but also leads to the decrease of parameter Q in Eq. (2) and then reduces the light yield [127]. In the simplest case of an exponential decay, the XEOL intensity I(t) is

$$I(t) \sim \exp[-t/\tau] \tag{3}$$

where τ is called the decay time [103]. For parity and/or spin forbidden transitions of most trivalent lanthanide activators, the decay times are typically several tens of μs up to ms. In the case of allowed 5d-4f transitions, such as in Ce^{3+} and Eu^{2+}, the decay times are down to tens of ns [101]. Both short response time and fast decay rate are essential for dynamic real-time X-ray imaging in some specific medical diagnostics such as CT.

Spatial resolution: The spatial resolution represents the contrast and the amount of blurs over a certain range of spatial frequencies of an image, which is generally evaluated by the modulation transfer function (MTF) [128]. A thinner scintillation layer benefits the realization of high spatial resolution, while a thicker one can improve the X-ray blocking ability [129]. Thus, the thickness of a scintillation layer should be optimized in practical applications.

Chemical stability and radiation resistance. Chemical stability is mainly referring to the hygroscopicity of scintillators, which determines their longtime operation in the open air environment. Radiation resistance of scintillators regards mainly the variation and instability of the performances upon long-time X-ray irradiation [103]. The microstructure of fluoride NSs, especially the surface coordination environment, can greatly influence their scintillation performances, which should be regarded as an important stability parameter.

Furthermore, for some specific applications, the linearity of XEOL response with the incident X-ray dose and intensity, the emission wavelength, the energy resolution and the cost are important criteria for the selection of scintillators as well [108, 122]. For dynamic real-time X-ray imaging, the afterglow of a scintillator should be restricted to avoid sickle artifacts [4].

3 Photon conversion and mechanisms in lanthanide doped fluoride NSs

Lanthanide doped fluoride NSs have been widely studied in the NIR-triggered UC and UV-excited DS fields [130–132], and have recently attracted great interests in the scintillation field [133, 134]. Although the final scintillation profiles of lanthanide activators are similar to those reported in UC and DS emissions, the electron population pathways to the excited levels are significantly different [134]. Owing to the high energy of X-ray photons and various possible scintillation processes, all the trivalent lanthanide activators from Ce^{3+} to Yb^{3+} except

Pm^{3+} ions can be activated by X-rays. Thus, the XEOL emission wavelengths covering from UV, to visible and to NIR are achieved through doping appropriate lanthanide activators [126, 135]. In addition, employing a tetragonal matrix with a low crystal symmetry which benefits the energy level splitting, the XEOL spectra at room temperature might be used for the analysis of electronic fine structures of lanthanide activators [134]. The main emitting levels of various lanthanide activators are schematically illustrated in Fig. 2 [136–139]. Typically, with employing the low frequency phonon crystal lattices of fluorides as hosts, Ce^{3+}, Pr^{3+}, Nd^{3+} and Gd^{3+} ions can emit UV photons, Pr^{3+}, Nd^{3+}, Sm^{3+}, Eu^{3+}, Tb^{3+}, Dy^{3+} Ho^{3+}, Er^{3+}, and Tm^{3+} ions can emit visible photons, Nd^{3+}, Ho^{3+}, Er^{3+}, Tm^{3+} and Yb^{3+} ions can emit NIR photons.

3.1 Mechanisms of XEOL processes in lanthanide doped fluoride NSs

The role of X-ray can be classified into chemical, biological, and physical effects such as penetration, ionization, fluorescence, thermal as well as optical interference, diffraction, reflection and refraction [140–143]. The interaction between X-rays and matter through an ionization process consists of photoelectric effect, Compton scattering, Thomson scattering, Rayleigh scattering and electron pair effect. Upon X-ray irradiation, an electron in the inner shell of an atom is excited and then escapes out of

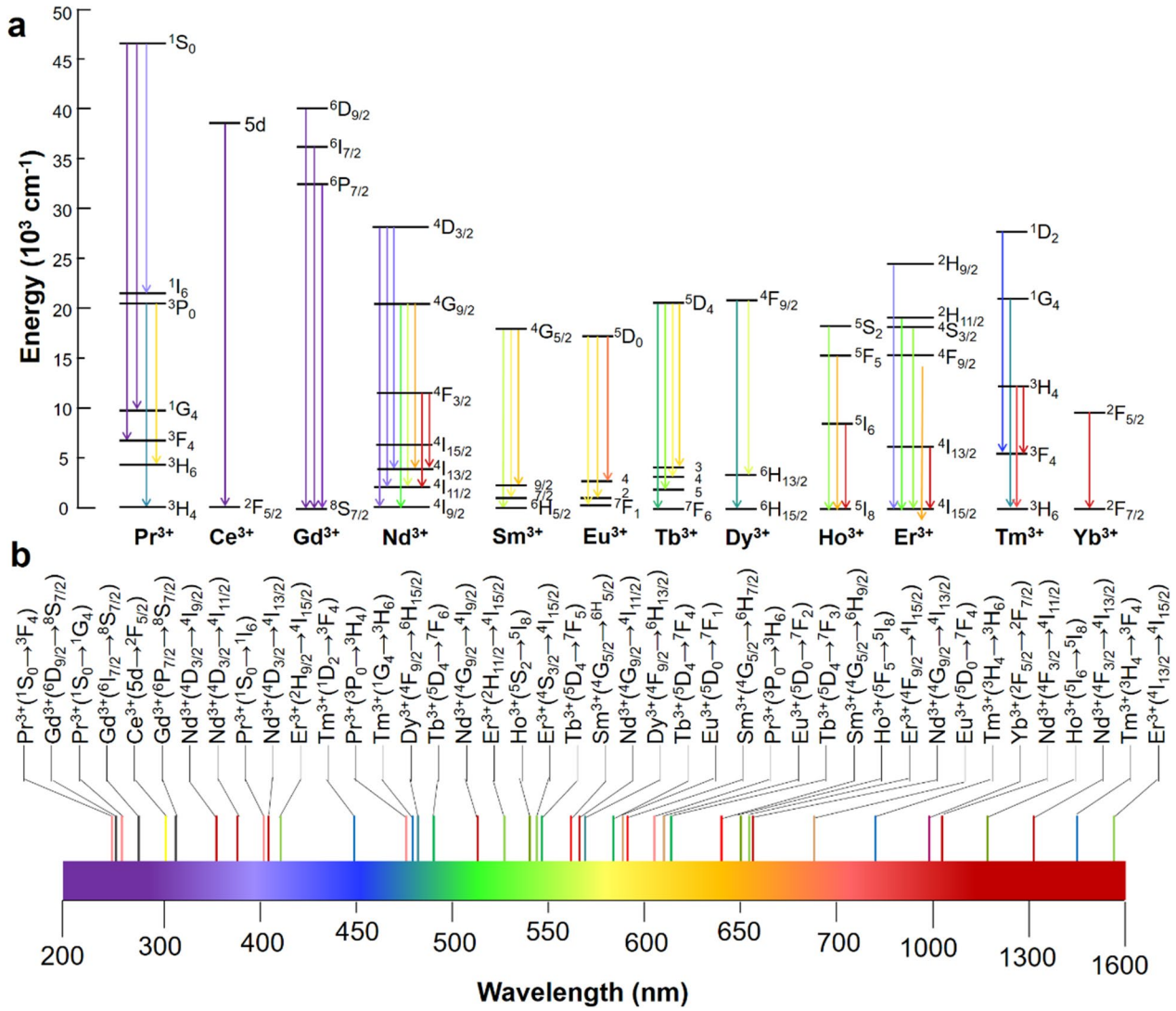

Fig. 2 **a** Partial 4f-energy level diagram for trivalent lanthanide activators. **b** Main luminescent transitions of the lanthanide activators in the electromagnetic spectrum

the atom, which is known as the photoelectric effect and is dominated when the incident X-ray photon energy is below ~500 keV [144]. When the incident X-rays with photon energy from a few hundred keV to several MeV interact with matter, both the energy and the direction are changed, a phenomenon which was first discovered by Arthur Holly Compton in 1923 and then named as Compton scattering [109, 145]. In contrast, Thomson scattering is an elastic and coherent interaction, which occurs between a low energy photon and a single free electron [146]. Rayleigh scattering is the superposition of multiple Thomson scattering, in which the incident photon energy is not changed but its directions is altered [147]. Both the Thomson scattering and Rayleigh scattering decrease with an increase of the irradiation energy. The electron pair effect represents the generation of a positive and negative electron pair during the interaction between the incident X-ray photons and the nucleus of an atom, which happens when the irradiation energy is over 1.02 MeV. Generated by the X-ray of 1.02 MeV, one positive electron interacts with a surrounding negative electron via annihilation generating two photons with the energy of 0.51 MeV [148–150].

The XEOL processes in lanthanide doped fluoride NSs are similar to those of activators doped bulk scintillators, which mainly include three stages of conversion, transport and luminescence, as illustrated in Fig. 3 [60, 103]. Generally, the maximum X-ray photon energy is equal to the tube voltage multiplied by the electron charge. At the first stage of conversion, the incident X-ray photons interact with the lattice heavy atoms (i.e., Cs^{+}, Ba^{2+}, Ln^{3+}, Bi^{3+}) to generate hot electrons and deep holes, mainly through the photoelectric effect and Compton scattering effect. Massive secondary electrons are then produced via electron–electron scattering and the Auger process, resulting in the generation of lower kinetic energy charge carriers. These energetic charge carriers are thermally dissipated via interacting with phonons, and then a large amount of low energy electrons and holes are populated in the conduction band and valence band, respectively. This conversion stage takes place in subpicoseconds [109].

At the second stage of transport, the produced large number of electrons and holes are transported to luminescence centers, captured by defects such as ionic vacancies, surface defects or Frenkel defects, or be self-trapped in the crystal lattice. This process usually takes place in 10^{-12} ~ 10^{-8} s. The defects either increase the nonradiative possibilities of the lanthanide activators, which leads to the decrease of XEOL intensity, or contribute to the production of afterglow [44]. Generally, limited afterglow benefits the increase of the signal-to-noise ratio and then produces high contrast images without lag, which is of significance for real-time dynamic XEOL imaging [105, 106]. However, bright and long XEPL show promising application in biomedicine, which will be discussed in the application section.

At the last stage of luminescence, after the excited levels of lanthanide activators are populated via the absorption of energy from the recombination of the low kinetic energy carriers, XEOL is generated through 5d-4f or 4f-4f transitions. It is emphasized that the electrons deposited in the defect states can migrate to the excited levels through energy tunneling during X-ray irradiation, which will influence the continuous XEOL stability [44, 151]. Different from traditional bulk scintillators and metal halide NSs, it is facile to introduce energy transfer processes in lanthanide doped fluoride NSs via

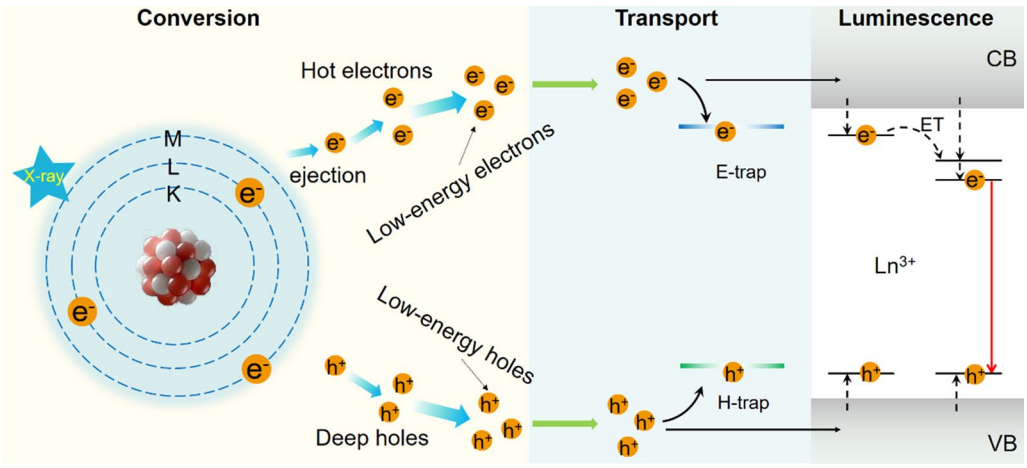

Fig. 3 Schematic illustration of the scintillation process in lanthanide doped fluoride NSs. CB, conduction band. VB, valence band. ET, energy transfer between lanthanide ions [109]

a codoping strategy and inhibit energy migration from activators to surface quenchers through coating shells, so as to improve the XEOL intensity [152, 153]. Moreover, through doping multiple activators in different layers of core/multi-shell fluoride NSs, multiple emission wavelengths produced by upconversion as well as down shifting can be realized, but it has not been extensively studied in XEOL until now.

3.2 X-ray to UV

UV emissions in lanthanide ions are mainly originated from the 5d-4f transitions, such as in Ce^{3+} and Pr^{3+} [122, 154]. The Ce^{3+} ion with the $4f^1$ configuration shows efficient broadband emission corresponding to the 5d-4f parity allowed electric dipole transition. The energy gap between the 4f ground state and the 5d excited state of the free Ce^{3+} ion is about 6.2 eV (50 000 cm^{-1}) [155, 156]. Since the 5d orbitals are susceptible to their surrounding crystal field, the symmetry, the anion polarizability, covalence and the surrounding surface ligands, the excitation and the emission wavelengths can be modulated by changing the chemical composition and the structure of the hosts [122, 157]. In common fluoride crystals, such as alkali/alkaline-earth rare-earth fluorides, or alkaline-earth fluorides, the doped Ce^{3+} ions are generally used to absorb the UV photons via 4f-5d transition and then sensitize Sm^{3+}, Eu^{3+}, Tb^{3+} and Dy^{3+} ions [158, 159]. Upon X-ray irradiation, the broad UV emission in Ce^{3+} from 280 to 350 nm, which contains two emission peaks of ~ 308 nm originated from $5d \rightarrow 4f$ ($^2F_{5/2}$) and ~ 325 nm originated from $5d \rightarrow 4f$ ($^2F_{7/2}$) transitions, was recorded in the tetragonal $LiYF_4$:Ce microcrystals. This strong UV emission was further used to activate wavelength shifters such as CdSe/ZnS quantum dots to modify the XEOL emission across the visible range. Their reported polymer composites were physical mixtures of $LiYF_4$:Ce microcrystals and CdSe/ZnS quantum dots [160]; a controlled synthesis of heterostrcutures between them might improve the XEOL intensity. For extending the XEOL wavelength to UVC range, the cubic elpasolite Cs_2NaYF_6 host with high defect-bearing characteristic was employed to incorporate Pr^{3+} ions. As a result, the UVC emission peaking at 250 nm corresponding to the Pr^{3+}: $4f5d \rightarrow {}^3H_4$ transition was achieved [161]. This reported Cs_2NaYF_6 host was synthesized via a solid state reaction where the structures such as size, shape and surface molecules were hard to be modified. In such case, the structure—XEOL property relationships in this host are not studied yet. In addition, in the LuF_3 [162] or $BaLu_2F_8$ [163] single crystal, sharp emission of Nd^{3+} (~ 170 nm) corresponding to the 5d-4f transition was observed.

Except 5d-4f transitions, the radiative transitions from high energy 4f levels can result in UV emission as well, such as in Gd^{3+} and Nd^{3+}. For example, in the hexagonal $NaLuF_4$:Gd/Tb NSs, the Gd^{3+} ions were used to promote the population of Tb^{3+} ions via energy transfer and then enhance the XEOL intensity, while its emission peaking at 311 nm corresponding to the $^6P_{7/2} \rightarrow {}^8S_{7/2}$ transition was recorded simultaneously. The XEOL intensity of Gd^{3+} ions were much weaker than that of Tb^{3+} ions, which might be attributed to energy transfer from Gd^{3+} to Tb^{3+}. With codoping Gd^{3+}/Nd^{3+} ions in the $NaLuF_4$ NSs, the emission at 385 nm corresponding to Nd^{3+}: $^4D_{3/2} \rightarrow {}^4I_{11/2}$ transition was observed [44].

3.3 X-rays to visible

The 4f-4f transition in a $4f^N$ electronic configuration is in principle electric dipole forbidden by the Laporte's rule. However, since the sites occupied by lanthanide ions in the fluorides do not present a center of inversion, Laporte's rule is relaxed to some extent due to odd parity terms in the ligand field Hamiltonian [164]. Thus, various visible emissions in lanthanide ions corresponding to the 4f-4f transitions are observed after the absorption of X-rays, whose profiles are much similar to those of common UC and DS in luminescent materials. For examples, characteristic transitions originated from Tb^{3+} (green, $^5D_4 \rightarrow {}^7F_{3\text{-}6}$), Eu^{3+} (red, $^5D_0 \rightarrow {}^7F_{0\text{-}6}$) and Sm^{3+} (red, $^4G_{5/2} \rightarrow {}^6H_{5/2\text{–}11/2}$) ions were detected when employing the $NaLuF_4$ NSs as the host. The Tb^{3+} ion usually exhibits stronger XEOL intensity than those of Sm^{3+}, Eu^{3+} and Dy^{3+} ions in a same host [44, 165], and the green wavelength matches well with the visible photodetectors. Thus, Tb^{3+} ions incorporated scintillators are broadly studied [44].

Similar to the Ce^{3+}-sensitized DS luminescent materials, Gd^{3+} ions might be used as efficient bridge centers to improve the XEOL intensities of Tb^{3+}, Sm^{3+}, Eu^{3+} and Dy^{3+} ions as well [108]. Because X-ray photons possess much higher energy than that of UV photons, the strong XEOL emissions of Er^{3+}, Ho^{3+} and Tm^{3+}, which are widely used in UC materials, are easier to be recorded in the doped $NaLuF_4$ NSs. Compared with bulk materials, NSs have a larger surface-to-volume ratio and more surface defects [166, 167]. Building a core@shell architecture has been verified to be an effective route to restrict the energy migration from activators to surface quenchers, followed by the decreased nonradiative transition possibilities and improved luminescence intensity [140, 168, 169]. The influence of shell thickness on UC and XEOL is quite different. For the Yb/Tm: $NaYF_4$ NSs with a mean particle size of 30 nm, the optimal $NaYF_4$ shell thickness for bright UC emission intensity but small size was found to be about 6.3 nm [170]; for the Yb/Er: $NaYF_4$ NSs (ellipsoids with a length of ~25 nm and a width of ~21 nm), the optimal $NaYF_4$ shell thickness was about 5.5 nm [171].

It should be noted that the UC emission intensities did not decrease with further increasing the shell thickness over the optimal value. However, it was reported that the XEOL intensity of Eu^{3+} ions doped LuF_3 NSs (~4.4 nm) was evidently decreased when the LuF_3 shell thickness increased over ~1 nm [172]. Although it was previously speculated that a thicker shell could increase the fraction of non-emissive volume in the NSs and then lower the probability of radiative recombination of charge carriers at the luminescent centers followed by the decreased of XEOL intensity, but it still needs more theoretical and experimental results to clarify this phenomenon.

3.4 X-rays to NIR

Under X-ray irradiation, NIR emissions originating from the Nd^{3+} ($^4F_{3/2} \rightarrow {}^4I_{9/2}$, ~866 nm/ ~893 nm; $^4F_{3/2} \rightarrow {}^4I_{11/2}$, ~1064 nm), Ho^{3+} ($^5I_6 \rightarrow {}^5I_8$, ~1180 nm), Er^{3+} ($^4I_{11/2} \rightarrow {}^4I_{15/2}$, ~980 nm; $^4I_{13/2} \rightarrow {}^4I_{15/2}$, ~1525 nm), Tm^{3+} ($^3H_4 \rightarrow {}^3H_6$, ~800 nm; $^1G_4 \rightarrow {}^3H_4$, ~1120 nm; $^3H_4 \rightarrow {}^3F_4$, ~1475 nm) and Yb^{3+} ($^2F_{5/2} \rightarrow {}^2F_{7/2}$, ~980 nm) ions were recorded by employing the $NaYF_4$ NSs as host [173]. NIR luminescence exhibits deeper penetration depth than those of UV/visible light, which is suitable for biomedical application. Achieving strong XEOL emission in the NIR range under a low irradiation dose is of significant importance from the view point of biosafety [174, 175]. Modulating the chemical compositions and constructing a core@shell structure in the lanthanide doped fluoride NSs are general feasible routes to enhance the XEOL emission intensity [42, 176]. Because the radiation energy of the recombination of charge carriers is much larger than that of NIR photons, the high energy levels of lanthanide activators are prior populated, and then multi-step nonradiation relaxations or cross-relaxations are required to produce NIR emissions [173]. Thus, introducing appropriate assisted energy levels to increase the electrons population in the low excited energy levels is a useful tool for the enhancement of XEOL emission in the NIR range.

4 X-ray excited persistent luminescence

4.1 XEPL mechanisms

Long persistent luminescent materials, also known as afterglow luminescent materials, have attracted great attention over the past few decades [177]. Long persistent luminescence refers to an optical phenomenon in which the stored excitation energy in traps is released to produces UV, visible or NIR photons which lasts for minutes, hours or even days after ceasing the excitation. The formation of suitable charge carrier traps such as type, concentration and depth in the crystal structure plays a vital role in the XEPL process [178]. Anion Frenkel defects were recognized as traps in fluoride hosts, such as $NaLuF_4$ and $NaYF_4$. The dislocation of fluorine anions (F^-) to interstitial sites through elastic collisions with large-momentum X-ray photons leads to the formation of fluorine vacancies (E-traps) and interstitials (H-traps), accompanied by the production and trapping of many energetic electrons in Frenkel defect-related trap states [44, 151]. The XEPL mechanism in lanthanide doped fluoride NSs is illustrated in Fig. 4. The X-rays induced low kinetic energy electrons and holes in the conversion stage of the XEOL process are partially captured by the traps. After ceasing the X-rays, the captured electrons and holes are released from the traps to the conduction band and the valence band, respectively, due to stimulation by heat. The excited levels of lanthanide activators are then

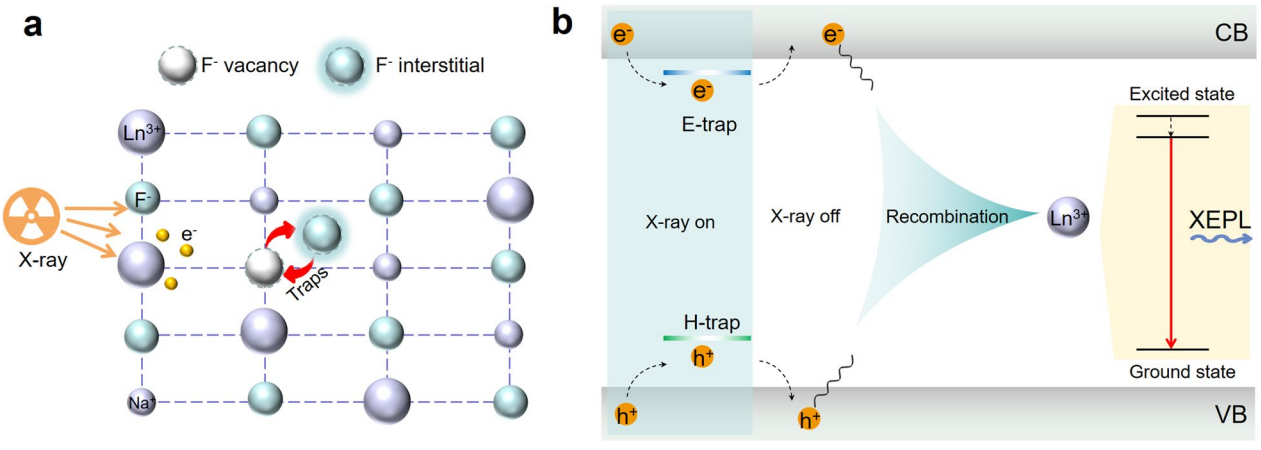

Fig. 4 **a** Schematic illustrating creation of Frenkel-related trap states in fluoride crystal lattices upon X-ray irradiation [44]. Copyright 2021 Springer Nature Limited. **b** The XEPL mechanism in lanthanide doped fluoride NSs [151]

populated via the recombination of these electrons and holes. Finally, the XEPL is generated through 5d-4f or 4f-4f transitions.

4.2 XEPL in fluoride hosts

UVC light in the 200–280 nm range shows the capability of germicidal activity, which can be used to kill bacteria, viruses, and other pathogens by destroying nucleic acids and disabling their ability to multiply [161, 179]. To generate UVC persistent luminescence, the host should have a large bandgap, thus, X-ray is appropriate as a stimuli source. The band gap of pristine Cs_2NaYF_6 is ~9.67 eV, which was verified to be suitable for the generation of XEPL in the UVC range from Pr^{3+} activators. As shown in the Fig. 5a, the XEPL peaking at 250 nm ($4f5d \rightarrow {}^3H_4$), 270 nm ($4f5d \rightarrow {}^3H_5$), 486 nm (${}^3P_0 \rightarrow {}^3H_4$) and 610 nm (${}^3P_0 \rightarrow {}^3H_6$) were recorded in the Cs_2NaYF_6: Pr^{3+}. The existence of fluorine vacancy-related defect levels was verified by density functional theory calculations and thermoluminescence analysis. The trap depths (E) relative to the conduction band minimum (CBM) was calculated by the formula of $E = 0.002T_m$, in which T_m is the temperature corresponding to the maximum thermoluminescence peak. Three shallow traps, with

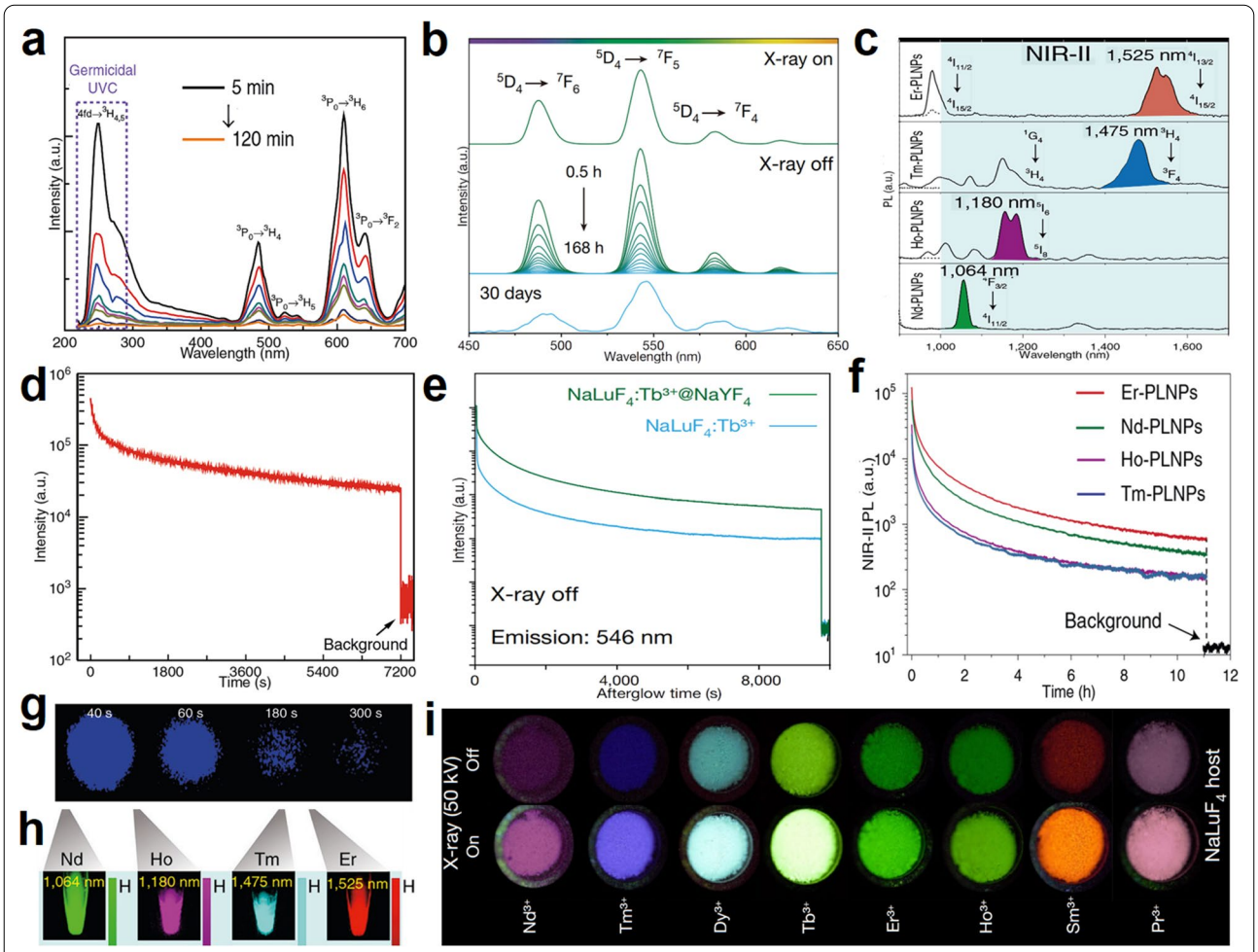

Fig. 5 **a** XEPL spectra of the $Cs_2NaY_{0.99}F_6$: $0.01Pr^{3+}$ recorded at different times [161]. Copyright 2018 Springer Nature Limited. **b** XEOL spectra of the $NaLuF_4$: Tb^{3+}@$NaYF_4$ core@shell nanocrystals, recorded after cessation of X-rays (50 kV) for 0.5–168 h or 30 days [44]. Copyright 2021 Springer Nature Limited. **c** Tunable XEPL spectra of lanthanide-doped $NaYF_4$ based core@shell NSs [173]. Copyright 2021 Springer Nature Limited. **d** XEPL decay curve of the $Cs_2NaY_{0.99}F_6$: $0.01Pr^{3+}$ detected at 250 nm [161]. Copyright 2018 Springer Nature Limited. **e** XEPL decay curve of the $NaLuF_4$:Tb^{3+} and $NaLuF_4$: Tb^{3+}@$NaYF_4$ nanocrystals monitored at 546 nm [44]. Copyright 2021 Springer Nature Limited. **f** NIR-II XEPL decay curves of typical emission bands of lanthanide-doped $NaYF_4$ based core@shell NSs [173]. Copyright 2021 Springer Nature Limited. **g** UVC images of the $Cs_2NaY_{0.99}F_6$: $0.01Pr^{3+}$ phosphors taken at different afterglow times [161]. Copyright 2018 Springer Nature Limited. **h** NIR-II XEPL images of lanthanide-doped $NaYF_4$ based core@shell NSs [173]. Copyright 2021 Springer Nature Limited. **i** XEOL and XEPL images of $NaLuF_4$ NSs doped with various activators [44]. Copyright 2021 Springer Nature Limited

respect to those > 1.3 eV below the CBM, were calculated to have the activation energies of 0.69, 0.83, and 1.02 eV at 70, 141, and 238 °C, respectively. The XEPL at 250 nm lasts over 2 h, and the intensity is still over one order of magnitude stronger than the background signal after 2 h (Fig. 5d, g). This XEPL intensity could be improved by tuning the Pr^{3+} ions concentration and the X-ray irradiation duration [122].

The XEPL in the visible range has been achieved in a series of trivalent lanthanides, such as Pr^{3+}, Nd^{3+}, Sm^{3+}, Tb^{3+}, Dy^{3+}, Ho^{3+}, Er^{3+} and Tm^{3+}. For example, a bright and ultra-long (over 30 days) green XEPL was reported in the $NaLuF_4$:Tb@$NaYF_4$ core@shell NSs with a mean particle size of 27 nm (Fig. 5b, i). After coating the shell, the XEOL and XEPL intensities were enhanced by 1.5-fold and 6.5-fold, respectively (Fig. 5e), both of which were much stronger than in the commercial plastic scintillators and conventional persistent phosphors, including $SrAl_2O_4$:Eu^{2+}/Dy^{3+} powder, ZnS:Cu^{2+}/Co^{2+} powder, $SrAl_2O_4$:Eu^{2+}/Dy^{3+} NSs and $ZnGa_2O_4$:Cr^{3+} NSs. First-principles calculations based on the density functional theory suggested that interstitial fluorine ions gradually diffuse back to original vacancies when the proximity between them is less than 3 Å. When the separation of these defect pairs is over 3 Å, the interstitial fluorine ions can be stabilized due to increased energy barriers, except under stimulation with heating or light exposure [44]. Similar to alkali rare-earth fluorides, the alkaline-earth fluorides are also used as hots for the realization of XEPL. The core CaF_2: Dy NSs (~ 13.1 nm) exhibited extremely weak XEPL, whose intensity was significantly enhanced after coating an inert $NaYF_4$ shell. Its intensity increased gradually with an increase of the shell thickness from 0.25 nm to 2 nm and then reached a plateau, but it was not evidently changed with tuning the shell compositions including $NaYF_4$, $NaYF_4$:Yb/Er, $NaYF_4$:Yb/Tm, $NaYF_4$:Ca, $NaGdF_4$, $NaYbF_4$ and $LiYF_4$ [180].

Through doping Nd^{3+}, Ho^{3+}, Er^{3+} or Tm^{3+} ions in the $NaYF_4$ or $NaGdF_4$ NSs, NIR-II XEPL were achieved, which lasted more than 72 h (Fig. 5c, f, h). The initial XEPL intensity enhanced with an increase of the X-ray dosage and reached a plateau at higher dosages of X-rays (> 200 Gy), which was probably due to a limitation in the harvesting of the excitation energy by the NSs. The morphology and the crystal structure showed high photostability during cycles of X-ray recharging. For the optimal $NaYF_4$:3Er@$NaYF_4$ NSs with 35 nm cores and 7 nm shells, its XEPL intensity was approximately 25-fold than that of the core NSs of 22 nm [173]. Comparison of afterglow duration in different lanthanide doped fluoride systems is shown in Table 1.

4.3 XEPL tuning strategies

The XEPL wavelength, intensity and duration should be modified to satisfy a specific application; for example, the XEPL intensity should be strictly limited for real-time dynamic imaging, but need to be strong enough for bio-sensing [176]. The 4f-4f transitions of lanthanide ions are almost independent of the local chemical environment owing to the shielding of 4f electrons by the outer 5s and 5p shells [122, 184], the XEPL wavelength is mainly tuned by doping different activators. It is possible to tune the XEPL wavelength of the Ce^{3+} ion by structural engineering because its 5d-4f transition is susceptible to the local environment [163]. There are several structural and external stimuli parameters which can be used to modify the XEPL intensity and duration: (1) A core@shell structure which is an effective route to passivate the NS surface defects and then enhance the XEPL intensity [180]; (2) Crystal phase of the host, i.e., the XEPL intensity of the $NaYF_4$:3Er in the hexagonal phase was more than ten times stronger than that in the cubic phase [165]; (3) Crystal structure of the host, i.e., with increasing the Gd^{3+} doping content in the $NaYF_4$:Gd/3Er@$NaYF_4$ from 0 to 97 mol%, the XEPL intensity first decreased and then increased, which might be ascribed to the increased lattice defects that origin from the atomic size mismatch between Gd^{3+} and Y^{3+} [173]. (4) The activators doping concentration, core size, shell thickness, irradiation dose and time, trap depth as well as storage temperature could also influence the XEPL [44]. (5) Codoping Ce^{3+} ions was used to reduce the electron population in the excited energy levels of lanthanide ions and then significant weaken the XEPL [108]. Accompany with these initial results, more efforts are needed to clarify the related mechanisms, and it is remaining a need

Table 1 Comparison of XEPL among various of lanthanide doped fluoride NSs

Materials	Afterglow color, duration	Materials	Afterglow color, duration
Na_3HfF_7:Yb/Er	Red, > 90 s [134]	Cs_2NaYF_6:Tb	Green, > 50 h [182]
$NaYF_4$:Tb@$NaYF_4$	Green, > 600 s [153]	$NaYF_4$:Er(Nd/Ho/Tm)@$NaYF_4$	NIR-II, > 72 h [173]
$NaMgF_3$:Tb@$NaMgF_3$	Green, > 10 min [181]	β-$NaYF_4$:Tb	Green, > 120 h [183]
Cs_2NaYF_6:Pr	UVC, > 2 h [161]	$NaLuF_4$:Tb@$NaYF_4$	Green, > 30 days [44]

to develop novel methods to significantly amplify or restrict the XEPL for specific applications.

4.4 Simultaneous XEOL, XEPL, UC and DS emissions using multiple shells

Lanthanide doped fluoride NSs have been broadly used to generate NIR triggered photon UC and UV excited DS emissions in addition to XEOL and XEPL (Fig. 6a) [130–132]. Core/multi-shells nanostructure can be employed to simultaneously produce XEOL, XEPL, as well as UC and DS, which allow researchers to manipulate the excitation dynamics of lanthanide activators. Because the electron population pathways in these processes are significantly different, several interesting physical processes such as excitation-dependent multiple emissions and thermal-response multicolors are facile to be manipulated. For example, when different lanthanide activators are used to generate diverse emission wavelengths of XEOL, UC and DS in core@shell@shell NSs (Fig. 6b), plentiful multicolors can be modulated on demand through controlling the excitation wavelength and/or power, which show promising applications in dynamic display and multi-level anti-counterfeiting. It should be noted that the relative intensities of XEOL, UC and DS can be tuned by changing the spatial distributions of the activators in core@shell@shell structures. Especially, through modulating the incident photons at different timescale based on a specific requirement, time-response characteristic transitions can be designed, which show promising in multi-mode bio-imaging and bio-sensing.

5 Applications

5.1 XEOL imaging

The fundamental working principle of XEOL imaging is to record the attenuation of X-rays after penetrating the specific subjects by using a scintillator and then imaging with a camera (Fig. 7). The scintillator screen is placed under the target to absorb the transmitted X-ray photons. For examples, a low dose of X-rays penetrating live organisms enables the application of computed tomography, while penetrating nonliving matter enables product quality and security inspection [7–16]. The X-ray

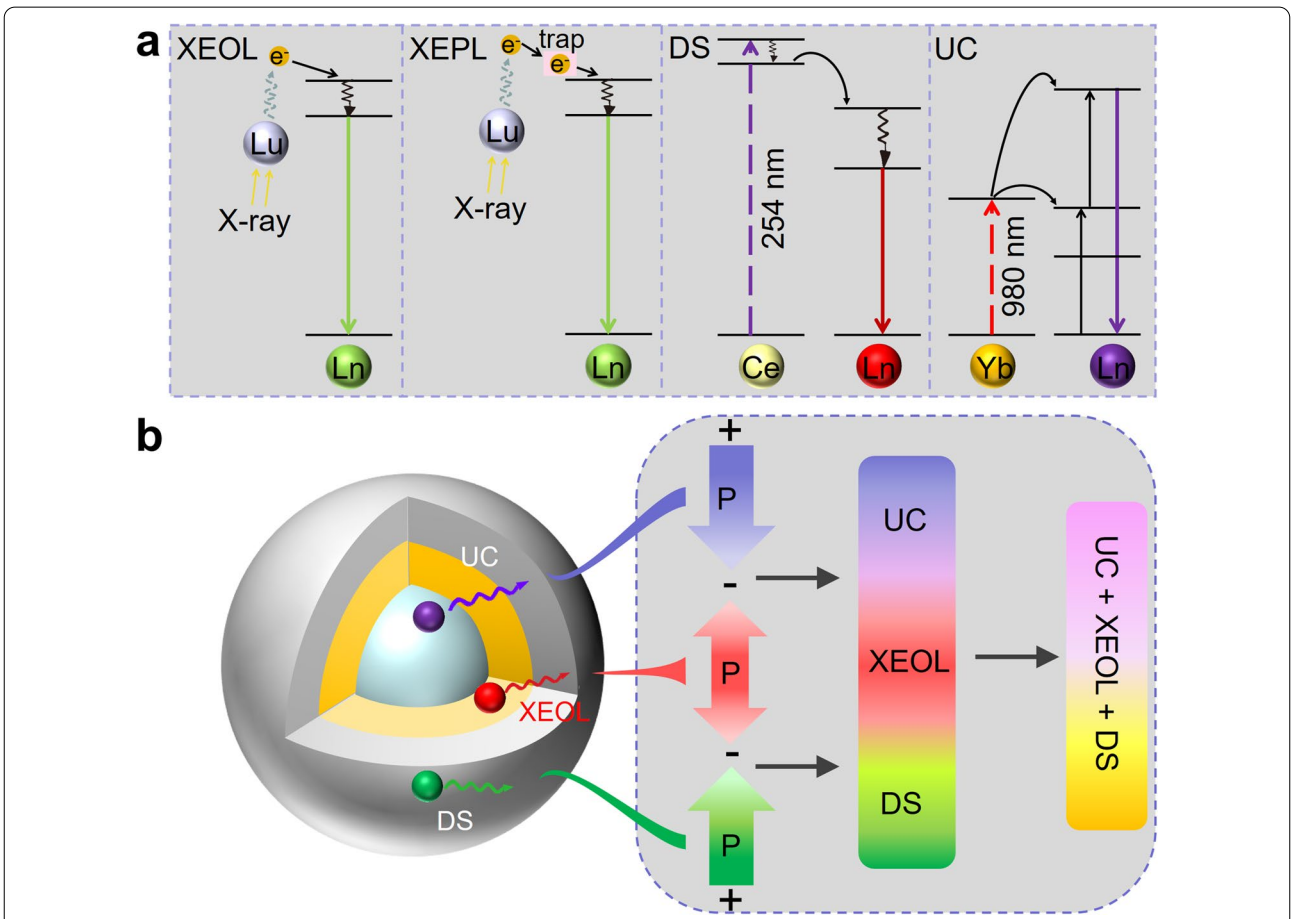

Fig. 6 **a** XEOL, XEPL, DS and UC processes in lanthanide doped fluoride NSs. **b** Schematic illustration of the multimode color evolution based on fluoride core@shell@shell NSs. P represents excitation power

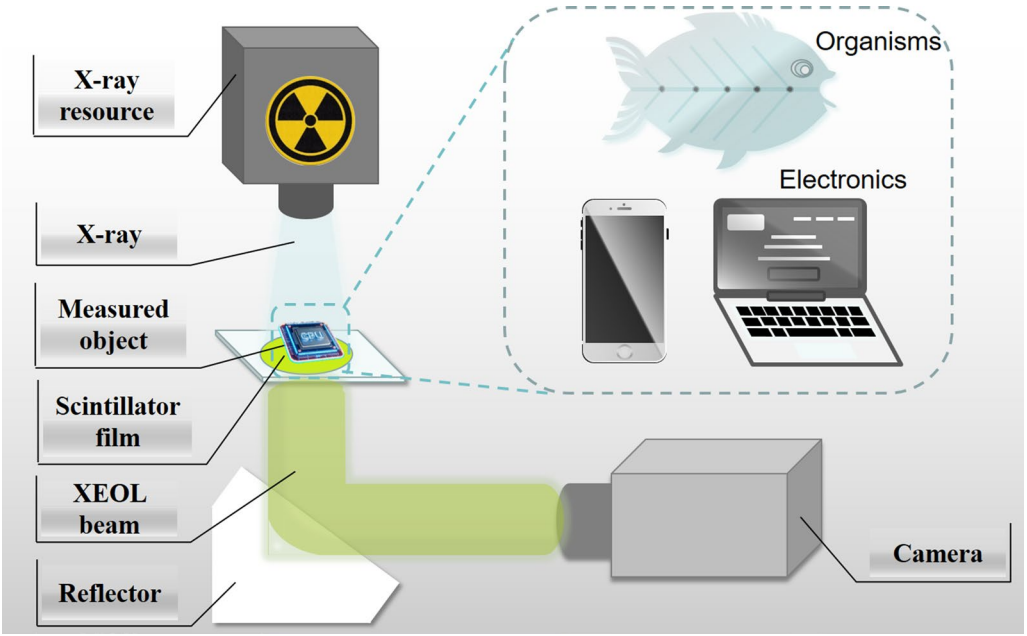

Fig. 7 Schematic illustration of the X-ray imaging system

irradiation dose should be low enough to assure the safety, while the high resolution and distinct contrast are important for image analysis. The maximum permissible dose for gonads and red bone marrow is ~ 5 rem/year; for skin, bone and thyroid is ~ 30 rem/year; for hands, forearms, feet and ankles is ~ 75 rem/ year; for any other single organ is ~ 15 rem/year [185].

The ethylenediaminetetraacetate (EDTA) capped $NaGdF_4$:Ce/Tb NSs exhibited reduced afterglow and highly efficient XEOL, which was demonstrated for high resolution XEOL imaging. The Ce^{3+} dopants can promote the energy migration from a trap center to surface quenchers via the Gd^{3+} sublattice and then greatly reduce the population in traps to produce weak afterglow. When employing an ultrathin transparent $NaGdF_4$: Ce/Tb involved film (0.045 mm) as a NS screen, a high spatial resolution of 18.6 lp mm^{-1} (lp: line pairs) was achieved. The MTF of a image is calculated by the slanted-edge method to reveal the spatial resolution [186, 187]. The spatial resolution is defined to be the spatial frequency at MTF = 0.2. The formula is as follows:

$$MTF(\nu) = F(LSF(x)) = F\left(\frac{dESF(x)}{dx}\right) \quad (4)$$

where ν is the spatial frequency, and x is the position of the pixels. The configuration inside of circuit boards with different electronic components, the thread of screw inside an opaque capsule, obvious biological tissue phase contrast and the bone shape of a chicken claw were clearly imaged by a simple XEOL imaging system (Fig. 8) [108]. It was reported that the $LiLuF_4$ possessed a higher absorption coefficient than those of CdTe, BaF_2, CdZnTe, and $CsPbBr_3$ materials at a higher photon energy, and the detection limit of $LiLuF_4$:15 Tb NSs was measured to be 36.31 nGy s^{-1}, which is much lower than typically used for X-ray diagnostics (5.50 μGy s^{-1}). The $LiLuF_4$:15 Tb NSs involved film was verified to be used for XEOL imaging to reveal the details of circuit board with a spatial resolution better than 20 lp mm^{-1} [188]. For dynamic real-time X-ray imaging, it remains a great challenge to develop divalent lanthanide or metal transition activators doped fluoride NSs with fast decay time.

Lanthanide-doped NSs featuring strong XEOL intensity and long XEPL were studied for X-ray luminescence extension imaging (Xr-LEI) as well (Fig. 9). By employing a flexible detector prepared by embedding $NaLuF_4$:15 Tb@$NaYF_4$ NSs into a polydimethylsiloxane (PDMS) substrate, the internal structures of a highly curved electronic circuit board was visualized and high-resolution 3D Xr-LEI was achieved though combining XEPL and graphical simulations, while only overlapped imaging of the electronic circuit board was recorded when using a typical flat-panel X-ray detector (Fig. 9c). The achieved spatial resolution was more than 20 lp mm^{-1}, which is much higher than that of conventional flat-panel X-ray detectors (typically less than 5 lp mm^{-1}) (Fig. 9e, f) [44]. Xr-LEI is an interesting and effective route to reveal the three dimensional

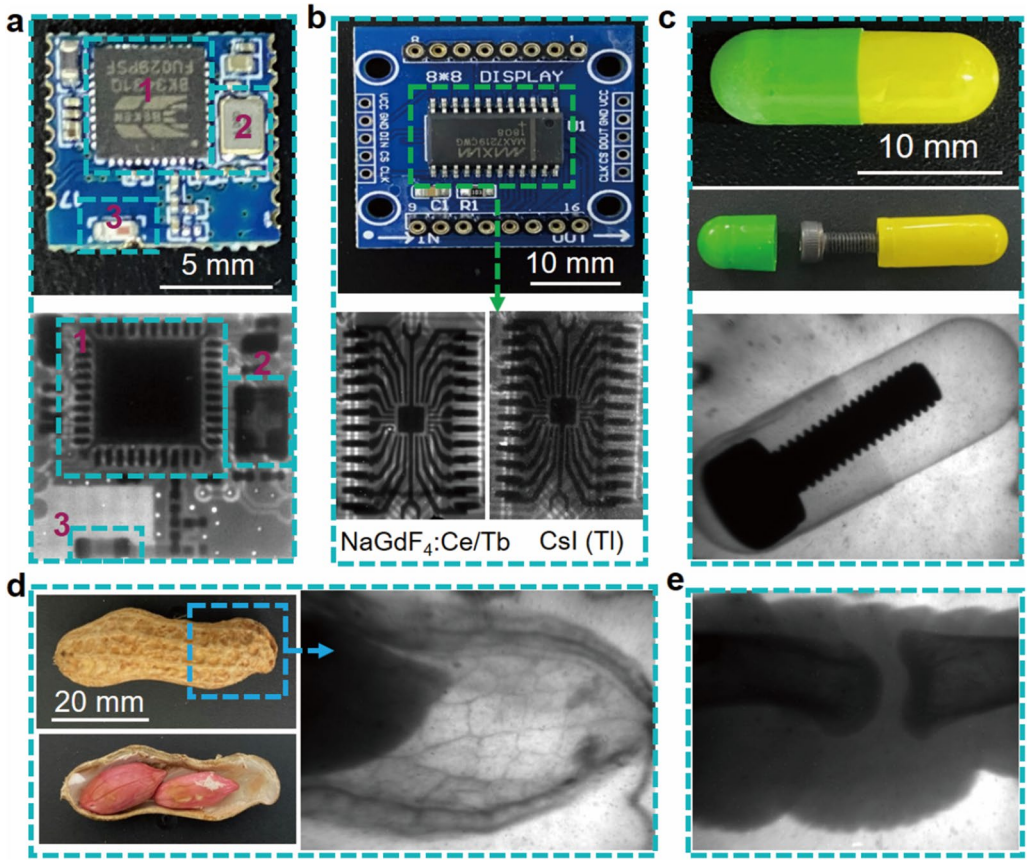

Fig. 8 **a** Photograph of a circuit board A (top) and its XEOL image (below). **b** Photograph of circuit board B (top), its XEOL images with using $NaGdF_4$: 10Ce/18 Tb film (below, left) and CsI (Tl) single crystal (below, right). **c** Photographs of a capsule containing a screw inside and its XEOL image. **d** Photographs of one peanut and its XEOL image. **e** XEOL image of a chicken claw. (dose rate: 42.08 $mGy_{air}\ s^{-1}$, voltage: 50 kV) [108]. Copyright 2021 American Chemical Society

structures of objects, which is inaccessible by conventional flat-panel X-ray detectors or synchrotron-based X-ray microscopy.

5.2 XEOL based biomedicine

X-ray, as an ionizing radiation with deep penetration depth in human body, has been broadly studied for radiotherapy and bioimaging applications [1–4, 167]. Benefiting from the feasible surface modification, various photosensitizers such as rose bengal (FDA-approved), verteporfin, ZnO, and choline e6 can be linked on the fluoride NSs via chemical conjugation or electrostatic adherence. The strong XEOL can activate the photosensitizers to generate reactive oxygen species, which then directly slow or even stop tumor growth by photodynamic therapy causing inflammation and compromising microvasculature [112].

The Ce^{3+} ions involved systems, such as CeF_3@verteporfin [189], CeF_3@ZnO [190], $CeLaF_3/LaF_3$@Chlorine e6 [191], CeF_3:Tb@CTAB-Chlorine e6 [192], CeF_3:Gd/Tb@rose Bengal [110], LaF_3:Tb@rose Bengal [193], $NaCeF_4$:Gd,Tb [152] NSs were widely studied in X-ray response biomedicine. Loading rose Bengal on the mesoporous silica-coated CeF_3:Gd/Tb NSs was used to generate efficient $^1O_2$ upon X-ray irradiation [112]. This product can be employed as a multifunctional tool capable of being used synergistically with dual-modal imaging (CT and magnetic resonance imaging), guided combined non-radioactive radiotherapy (RT) and X-Ray effected photodynamic therapy (XPDT) under a low X-ray irradiation dose. Combining synergistic RT + XPDT treatment modalities with untargeted global metabolomics can be used for the analysis of relevant metabolic tumor and serum biomarkers and their patterns. The synergistic RT + XPDT of $NaCeF_4$:Gd/Tb NSs showed better tumor inhibition efficiency than RT alone in both A549 lung tumor model and CT26 colon cancer model (Fig. 10) [152]. In addition, the $NaYF_4$:Gd/Tb NSs was reported as a light transducer for depth-independent NO release and on-demand gas-sensitized cancer therapy. Owing to the

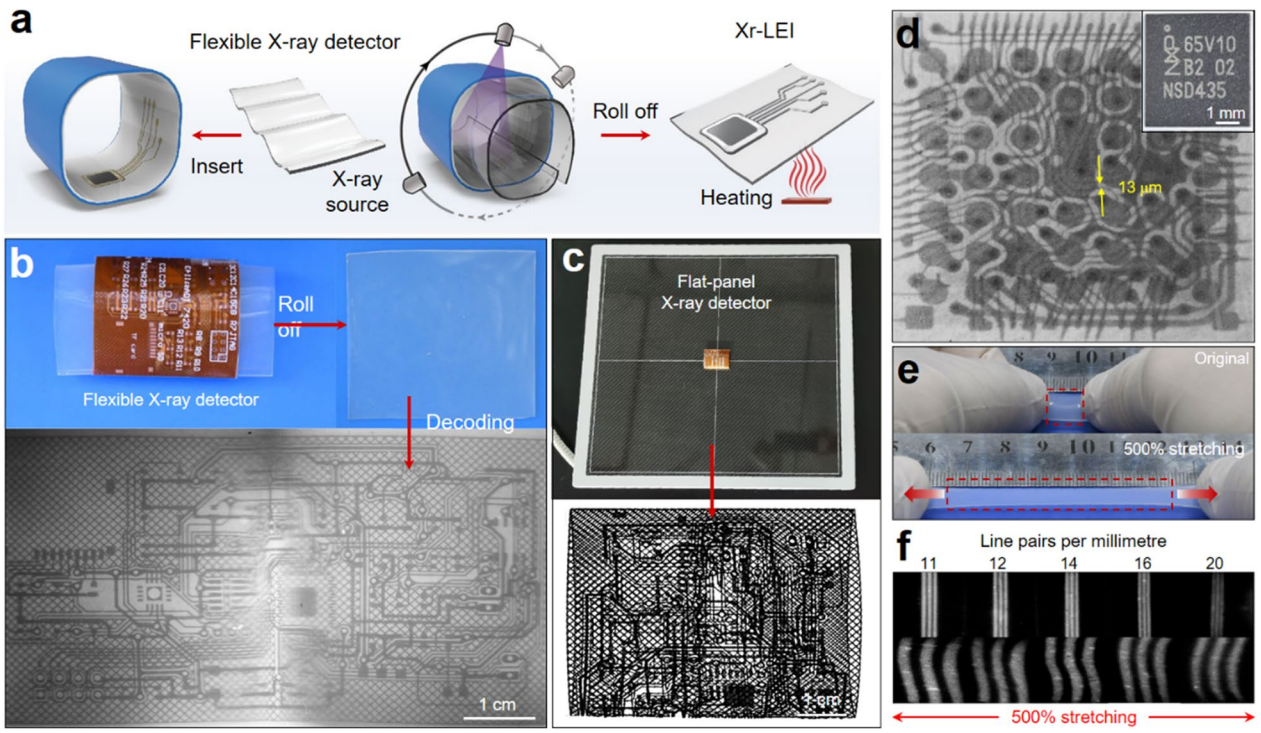

Fig. 9 **a** Schematic description of 3D electronic scintillation imaging through a NSs based stretchable X-ray detector. **b** Xr-LEI of a 3D circuit board by the $NaLuF_4$:Tb^{3+}(15 mol%)@$NaYF_4$ based flexible X-ray detector (50 kV, 80 °C). **c** X-ray imaging on the same electronic board by a traditional packaged flat panel detector. **d** Xr-LEI of inner circuits of an iPhone. Inset: digital photo of the same integrated circuits. **e** Photograph of the flexible scintillation layer. **f** High-quality Xr-LEI by applying the flexible X-ray detector [44]. Copyright 2021 Springer Nature Limited

energy transfer from $NaYF_4$:Gd/Tb NSs to the NO donor (RBS), ultralow soft X-ray dosage (~0.85 mGy) triggered NO release was realized in deep tissues even up to 3 cm depth, which broke the depth limitation suffered by the traditional UV/vis and NIR light. Upon X-ray irradiation, the $NaYF_4$:Gd/Tb-RBS agent could be used for the inhibition of tumor growth [194].

XEOL bio-medical imaging takes advantage over traditional fluorescence imaging due to the unlimited tissue penetration depth of X-rays. UV–vis and NIR can only penetrate a depth of 0.5–2.5 mm and 8–10 mm, respectively, while X-rays can easily reach several-centimeter penetration [176]. Although a great achievement has been achieved in the photoluminescence imaging field, some intrinsic disadvantages still exist, such as poor anatomical and physiological detail in vivo. Fluoride NSs can not only be used as CT contrast agents for CT imaging [195–198], but also employed for CT and photoluminescence imaging simultaneously to realize precision diagnosis. For example, $NaYF_4$:Nd^{3+}@$NaLuF_4$@polydopamine nanocomposites can be used in NIR-II optical and X-ray CT dual-modal imaging, which generated clearer in vivo tumor information than the gray-scale magnetic resonance imaging (Fig. 11a) [199]. Moreover, tri-model biological imaging was realized in the $NaGdF_4$:Yb,Tm@$NaGdF_4$ nanosystem. 980 nm laser activated energy transfer UC from Yb^{3+} to Tm^{3+} was used for high-resolution fluorescence imaging at the cellular level, X-ray CT was used for the revelation of tumor localization and magnetic resonance imaging originated from the paramagnetic Gd^{3+} ions was used for providing superior details and functional information about tissues (Fig. 11b) [200]. For the traditional bulk scintillators, in addition to the limitations discussed in the introduction section, they cannot be used for in vivo biomedicine. However, the bio-combinable lanthanide doped fluoride NSs show great promises in bio-medicine field. One of the most challenges is developing facile strategy to improve the LY, so as to reduce the employed dose rate of dangerous X-rays.

5.3 XEPL based biomedicine

The XEPL in UVC range can be used for sterilization and in vivo killing of pathogens and cancer cells [179]. Fluorides with large band gap and facile creation of anionic defects are appropriate for the generation of UVC persistent luminescence from 5d → 4f transitions of lanthanide activators. Through doping Pr^{3+} ions into the

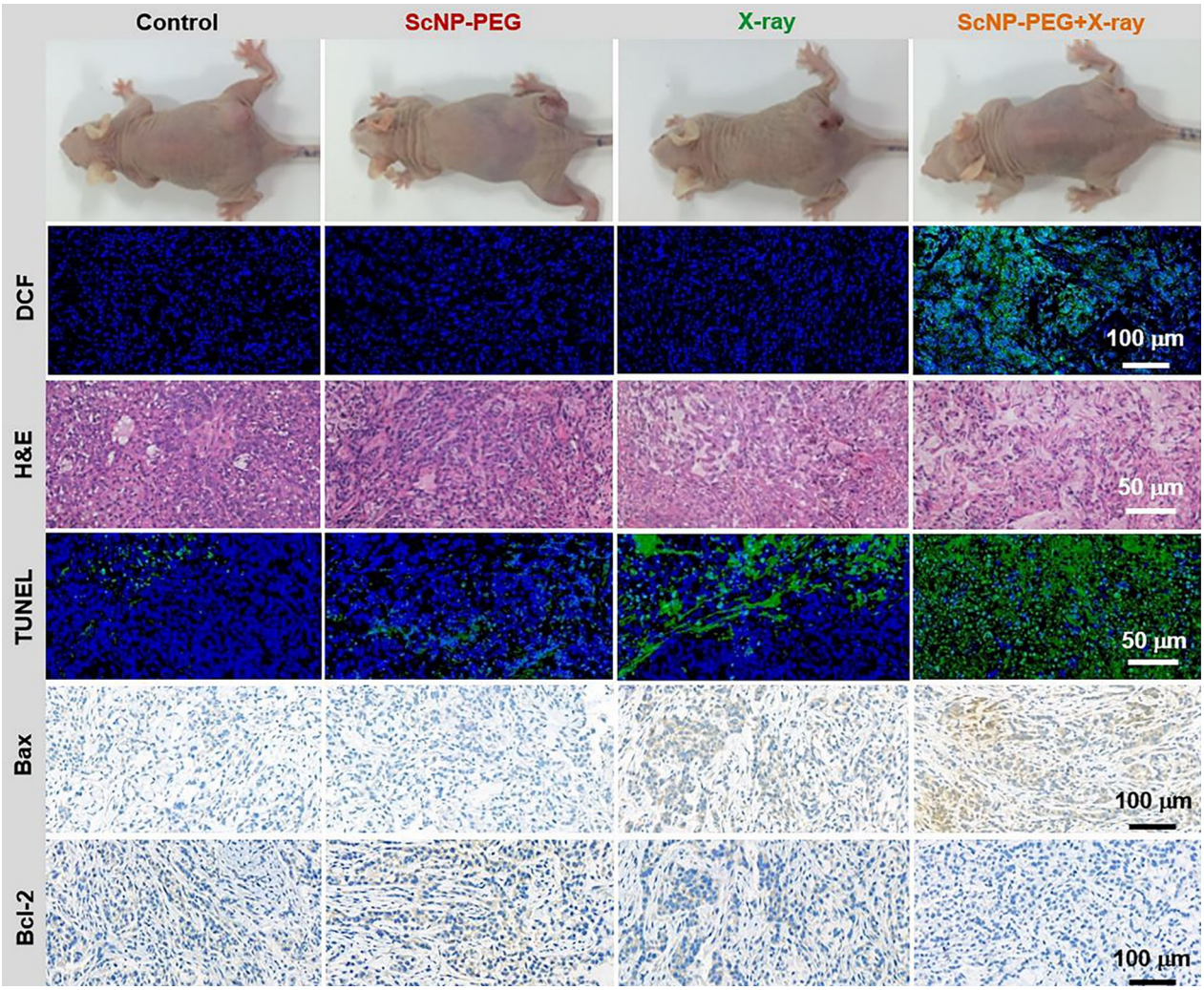

Fig. 10 Digital photographs of mice on the 30th day after different treatments, 2′,7′- dichlorofluorescein diacetate staining of A549 tumor for ROS (reactive oxygen species) visualization, images of Hematoxylin and eosin H&E and TdT-mediated dUTP nick end labeling stained tumor slices from different groups of mice and images of anti-Bax and anti-Bcl-2 stained tumor slices from different groups of mice from top to bottom. The energy and dose rate of X-ray were 160 kV and 1.103 Gy/min respectively [152]. Copyright 2019 American Chemical Society

defect-bearing cubic elpasolite Cs_2NaYF_6, bright XEPL peaking at ~ 250 nm ($4f5d \rightarrow {}^3H_4$) can last more than 2 h. Experimental characterizations combined with first-principles calculations suggested that oxygen introduction-induced fluorine vacancies acted as electron traps. As shown in Fig. 12a, 100% viability was maintained when keeping Pseudomonas aeruginosa PAO1 under ambient conditions (i.e., room light, normal atmosphere) for 30 min, while it was greatly decreased when increasing the XEPL intensity upon prolonging the irradiation time [161].

Tunable XEPL in the NIR-II window was realized in the $NaYF_4$: (Nd^{3+}, Ho^{3+}, Er^{3+} or Tm^{3+})@$NaYF_4$ core@shell NSs, which are promising for in vivo imaging applications, including high-contrast abdominal vessels, tumor imaging and ureter tracking, as well as multispectral in vivo deep-tissue viscera imaging and the multimodal XEPL-magnetic resonance-positron emission tomography imaging of tumors. As shown in the Fig. 12b, Er-doped NSs were first injected into a living mouse via the tail vein, followed by gavaging of Nd-doped NSs after 10 min; as a result, the overlayed NIR-II XEPL image clearly showed the main organs with a high contrast [173]. High resolution is significantly important in medical imaging. The full-width at half-maxima of 331.1 μm and 457.4 μm were achieved in the NIR-II XEPL imaging, which were 0.83-fold sharper than those obtained with NIR-II fluorescence imaging [173].

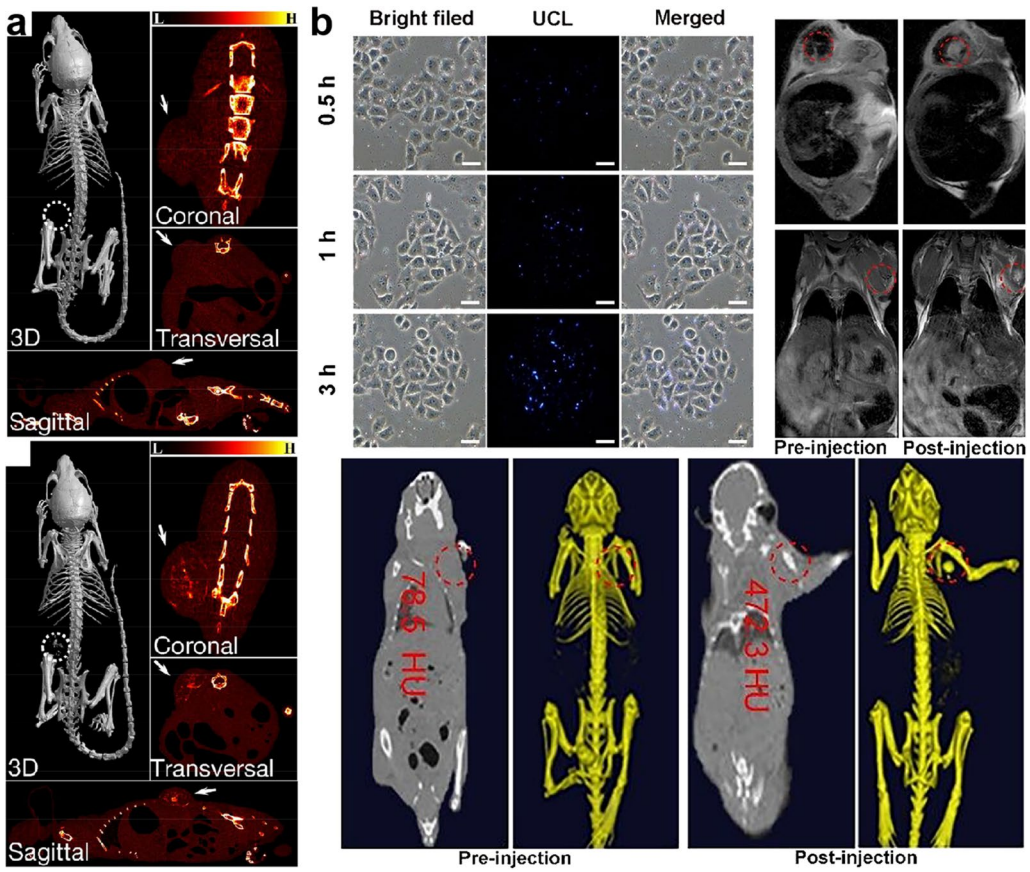

Fig. 11 **a** X-ray CT images of the HeLa tumors-bearing nude mice before (top) and after (bottom) intratumoral injection of $NaYF_4$:Nd^{3+}@$NaLuF_4$@polydopamine [199]. Copyright 2017 American Chemical Society **b**. UC images of HeLa cells incubated with $NaGdF_4$:Yb,Tm@$NaGdF_4$ at 37 °C for 0.5, 1, and 3 h. Scale bar: 50 μm (top left). In vivo T_1-weighted magnetic resonance images of tumor-bearing mice before and after injection (top right). In vivo CT images of a tumor-bearing mouse before and after injection (bottom) [200]. Copyright 2019 Royal Society of Chemistry

5.4 Information encoding

Fluoride NSs are one of most suitable hosts for UC, thus, dual optical properties of XEPL and upconvesion are facile to be realized by a core@shell structure, such as CaF_2:Dy@$NaYF_4$:Yb/Er and CaF_2:Dy@$NaYF_4$:Yb/Tm NSs, and time-dependent color evolution can be realized as well [180]. For example, in the Na_3HfF_7:Yb/Er NSs, the red UC intensity remained unchanged at a fixed pumping power and the bright green XEPL decreased gradually over time, which lead to the output color evolution from green to red naturally (Fig. 13a) [134]. Fluoride NSs prepared via wet-chemical method are well dispersed in a polar or nonpolar solvent, which are suitable for the design of patterns via printing and then employed for optical information storage. For example, $NaYF_4$:(Tb, Dy or Ho)@$NaYF_4$ with strong XEPL was printed on a glass sheet to form three quick-response codes, which was interpreted into three readable codes after passing through 545BP, 570BP, and 605LP optical filters (Fig. 13b) [153]. This route enables 3D information storage on a single layer of recording medium. Furthermore, the fluoride NSs could be used for information encryption and decryption. As shown in Fig. 13c a designed pattern with employing $NaMgF_3$:Tb^{3+}@$NaMgF_3$ NSs was clearly observed under X-ray irradiation and then faded once the cessation of excitation source. After heating several seconds, the stored pattern appeared again (Fig. 13c) [181]. Considering the UC and DS fluoride nanosystems show promising application in information encryption and encoding [201, 202], the combination of XEOL, XEPL, UC and DS may greatly improve the security level.

5.5 Broadband photodetection

Photodetectors have a wide range of applications in biomedical sensing [203, 204], camera imaging [205, 206], optical communications [207, 208], and night vision [209, 210]. In commercial photodetectors, crystalline inorganic semiconductors such as silicon or III-V compounds are employed as photodiodes and phototransistors, which do not effectively respond to a

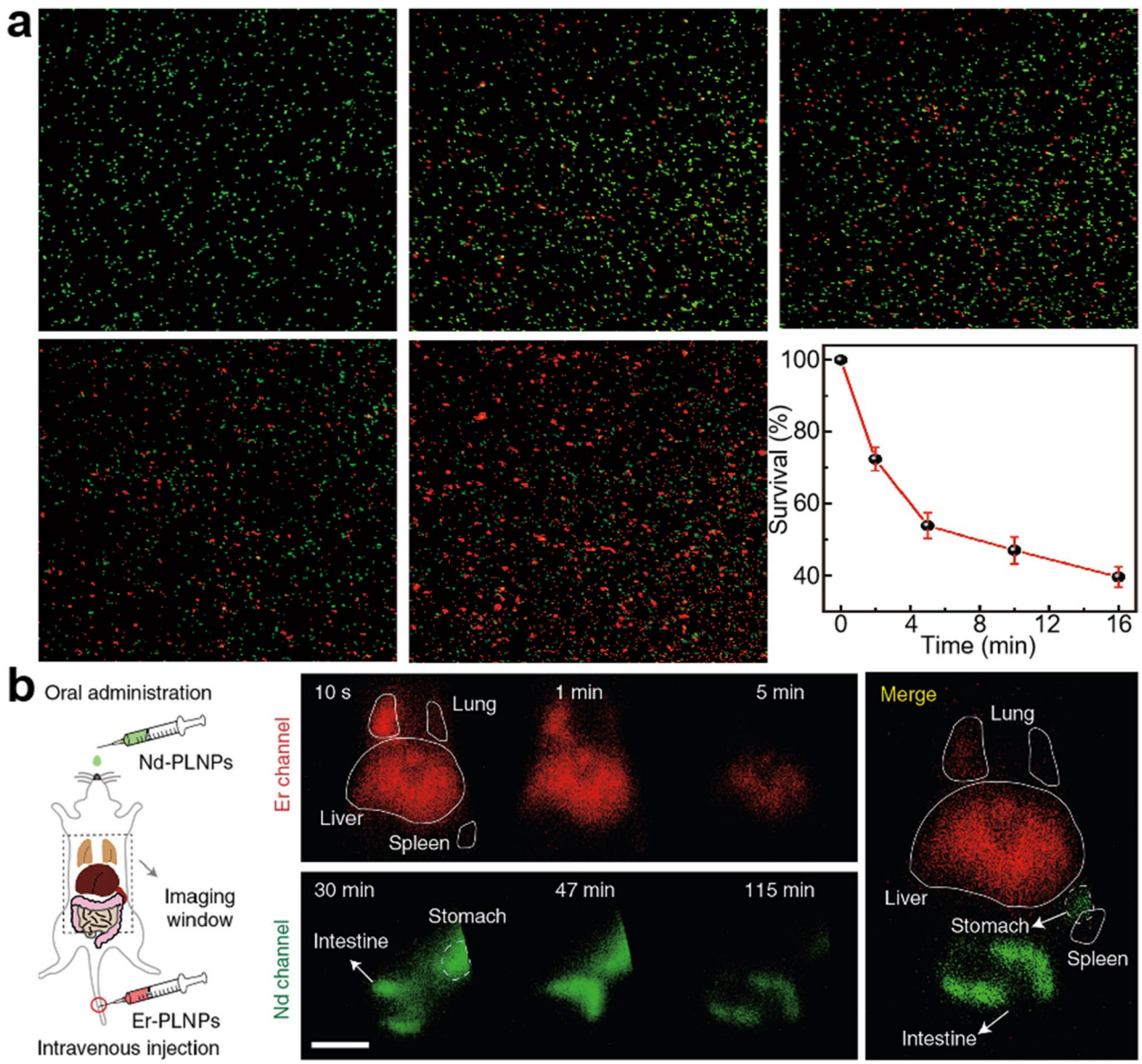

Fig. 12 **a** Inactivation of P. aeruginosa PAO1 using UVC-afterglow phosphor sheets. They were the control sample, irradiated by X-ray for 2 min, 5 min, 10 min, 16 min to inactivate *P. aeruginosa* PAO1 and the dependence of *P. aeruginosa* PAO1 survival ratios on the X-ray irradiation time of the given phosphor sheets, respectively. The live and dead cells show green and red colors, respectively [161]. Copyright 2018 Springer Nature Limited. **b** Dual-channel in vivo PL imaging of organs in a living mouse. Nd-doped NSs were used to image the gastrointestinal tract through oral administration, and Er-doped NSs were used to image visceral organs via a tail vein injection. Scale bar, 1 cm [173]. Copyright 2021 Springer Nature Limited

broad scope of photon energy covering X-ray, ultraviolet–visible (UV–vis), and NIR light [211]. To solve this issue, $NaYF_4$:Yb/Tm (30/1 mol%)@$NaYF_4$@$mSiO_2$@$MAPbX_3$ core@shell nanoparticles were developed. As shown in Fig. 14, under NIR excitation, lanthanide-doped fluoride layer emitted UV–vis light through energy-transfer UC processes, and then the subsequential radiation re-absorption process from lanthanide activators to perovskite layer occurs. Upon X-ray or UV excitation, visible emission from perovskite layer is produced through recombination of electrons in the CB and holes in the VB [212]. This nanotransducer exhibited a wide linear response to X-rays with various dose rates, as well as UV and NIR photons at different power densities. As discussed in Sect. 4.4, without integrating perovskite layer, lanthanide-doped fluoride NSs

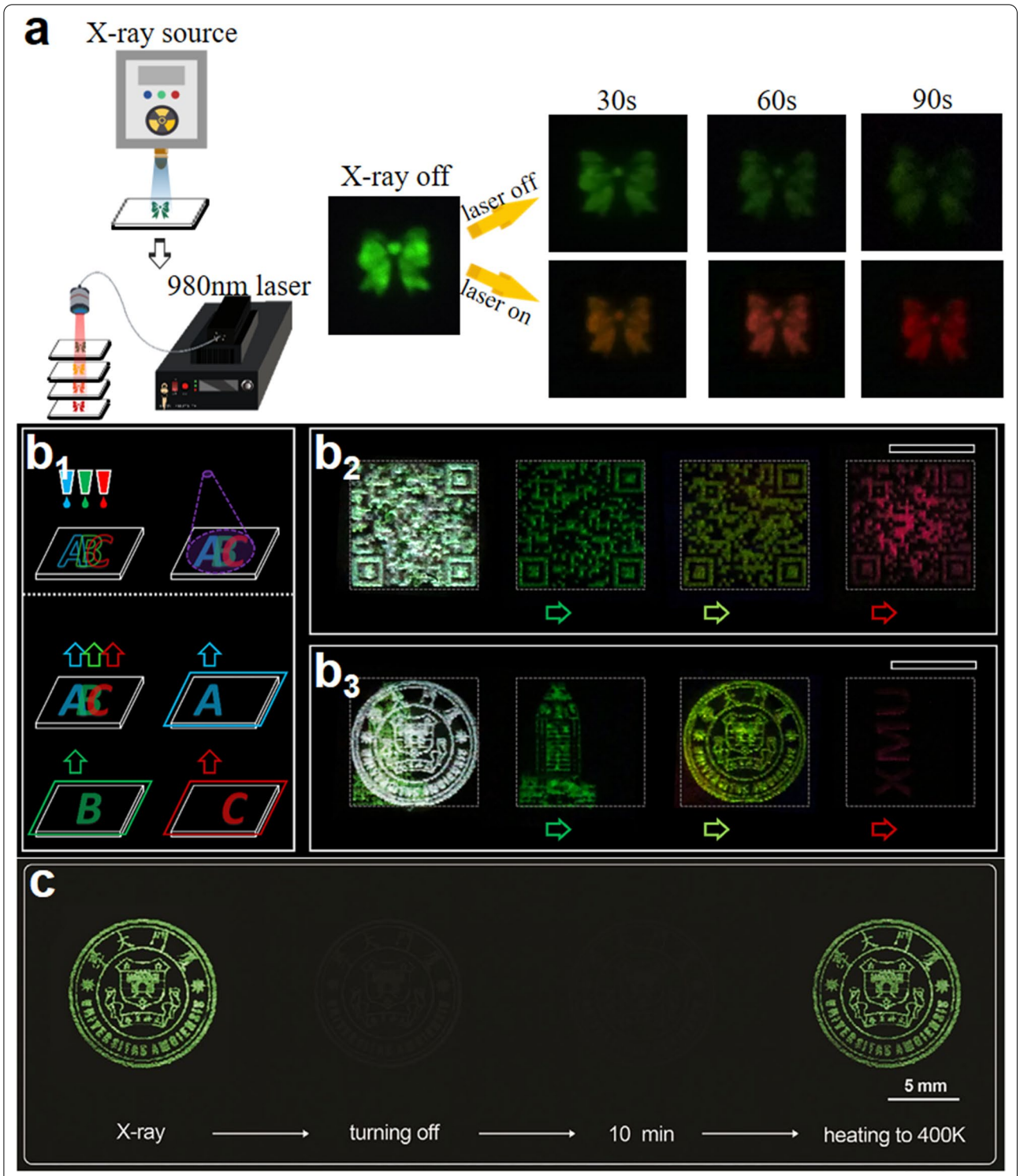

Fig. 13 **a** Schematic illustration for the realization of a time-dependent color variation display [134]. Copyright 2021 Royal Society of Chemistry. $\mathbf{b_1}$ Schematic illustration of the application in 3D optical information storage. $\mathbf{b_2}$-$\mathbf{b_3}$ The original images using $NaYF_4$:Ln^{3+}@$NaYF_4$ and monochromatic images after passing through 545BP, 570BP and 605LP filters. The scale bars are 100 μm [153]. Copyright 2021 Springer Nature Limited. **c** Photographs of $NaMgF_3$:Tb^{3+}@$NaMgF_3$ emission images during X-ray irradiation, at the moment of turning off, with a delay time of 10 min, and heated to 400 K [181]. Copyright 2021 Wiley–VCH

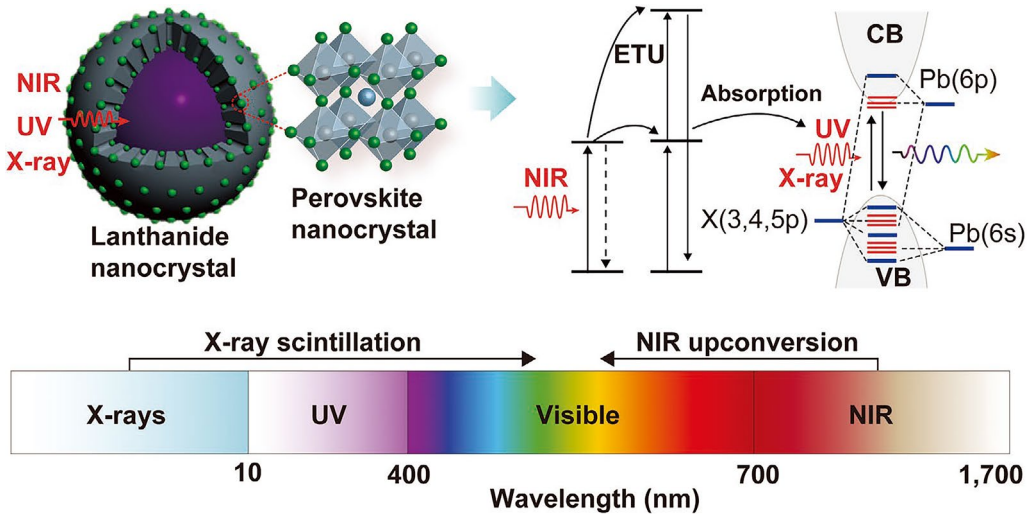

Fig. 14 Schematic illustration of the structure design of lanthanide-perovskite core@shell nanoparticles for detection of X-ray, UV, and NIR photons. Lanthanide doped upconversion nanocrystals are coated with a layer of $mSiO_2$ shell and organic–inorganic lead-halide perovskite nanocrystals are in situ synthesized inside the pores of mesoporous $mSiO_2$ [212]. Copyright 2021 Wiley–VCH

can be used for the generation of XEOL, UC and DS as well, which might be possible for the realization of broadband detection in theory and need more study in the future.

6 Existing challenges and future opportunities

Lanthanide doped fluoride nanoparticles are suitable candidates for next generation NSs owing to their low bio-toxicity, high photo-/environmental- stability, facile device processability, tunable XEOL and XEPL properties, and other useful features [44, 112–114]. To promote the development of high performance fluoride NSs and the practical applications, we further discuss the existing challenges and future multidisciplinary opportunities in this field below.

Understanding the XEOL mechanism benefits the design and exploration of new fluoride NSs. At present, how the generated low kinetic energy charge carriers are transported to the luminescent centers or are captured by defects as well as the corresponding influence factors, are unclear. For example, it is better to calculate or characterize the energy differences among these charge carries, the first populated nonradiative excited levels and the radiative levels of lanthanide activators, which will guide the design of energy transfer processes to match the energy differences followed by the enhanced light yield. High LY is a perquisite for the realization of ultra-low dose rate applications.

The life-times of 4f-4f transitions in most trivalent lanthanide ions vary from a few μs to tens of ms [213, 214], which are not suitable for real-time dynamic XEOL imaging. Although the decay rate of Ce^{3+} ions is in the nanosecond range, XEOL emission in fluoride NSs doped by cerium ions is in the UV region [188, 189], which do not match well with commonly used visible detectors. So to achieve bright XEOL intensity with fast decay rate and appropriate emission wavelength range, it is better to design the local crystal environment of 5d orbitals of Ce^{3+} and Eu^{2+} ions in fluoride NSs for the realization of better XEOL performances.

Scintillators with the quantum-cutting process, which take place in some lattices, have promising properties for a number application due to high quantum efficiency (up to 190%) of resulted visible emission. An example of well-investigated material is $LiGdF_4$ doped with Eu^{3+}, where Gd^{3+} acts as an intermediator of UV photon to Eu^{3+}, where quantum cutting occurs [215]. In addition, quantum cutting of UV photon is efficient in Tb^{3+} via cross-relaxation energy transfers between Tb^{3+} ions, leading to intense green emission [216]. Apparently, next step in this direction would be XEOL materials, where quantum cutting results to produce a pair of visible/NIR, or NIR/NIR photons, which can be realized in the lanthanide doped fluoride NSs [173]. However, it is remaining a great challenge to develop an effective method to improve its LY, owing to the big energy differences between the generated low secondary electrons and NIR excited levels. Quantum cutting processes via Pr^{3+}/Yb^{3+}, Tb^{3+}/Yb^{3+} or Ce^{3+}/Nd^{3+} co-dopants might be helpful for the increase of LY in NIR range, which is a promising research direction.

Through incorporating multiple lanthanide activators into fluoride based core@shell NSs, broadband photon detectors covering X-ray, UV–vis, and NIR light might be realized, which has not been studied yet. To inhibit deleterious cross-relaxations between different activators and achieve superior performances, the influences of activators type and their spatial distributions, the core@shell structures (i.e., composition, phase, shell thickness) and surface ligands are needed to be systematically studied.

The ability to trap X-ray photon energy in NSs for persistent radioluminescence, can be used in biomedical applications for wireless optogenetic control of neuron activities, cellular signaling pathways, and cell fate regulations. In this case, no real-time excitation would be required, thus causing less photodamage [173]. It is recognized that the XEPL is originated from the deposited electrons in defects that formduring X-rays irradiation [44, 151], however, it remains a challenge to clarify the influencing factors on the formation of defects and develop strategies to enhance the XEPL intensity and prolong its duration.

Both the fluoride host and scintillating screen structures are of significance for XEOL performance; it is thus valuable to study the structure dependent X-ray detection ability in the future. Most of the studies are mainly focused on the bulk scintillators or perovskite NSs, but scarcely in the fluoride based NSs field. Special structured scintillators with large radiation sensing area, composed of small units through meso- and macro- structure engineering [58], can exhibit extra-low level radiation sensitivity. Portable devices based on this technology could be useful for efficient remote environmental radiation monitoring.

The recent development of X-ray imaging technologies, including digital radiography, which in contrast to traditional film-screen radiography show a much wider and linear dynamic range and, therefore, reduces the risk of overexposure or underexposure [217]. This new technology inspires us to explore NSs based low-dose digital radiography in the future, and for proper processing and subsequent further analysis requires application of machine learning and artificial intelligence.

Abbreviations

XEOL: X-ray excited optical luminescence; GAGG:Ce: $Gd_3(Al,Ga)_5O_{12}$:Ce; NSs: Nanoscintillators; GSO:Ce: Gd_2SiO_5:Ce; XEPL: X-ray excited long persistent luminescence; LuAG:Ce: $Lu_3Al_5O_{12}$: Ce; UV: Ultraviolet; N_{ph}: Number of emitted photons; NIR: Near infrared; MTF: Modulation transfer function; CT: Computed tomography; E-traps: Fluorine vacancies; LYSO:Ce: $(Lu,Y)_2SiO_5$:Ce; H-traps: Fluorine interstitials; BGO: $Bi_4Ge_3O_{12}$; EDTA: Ethylenediaminetetraacetate; LY: Light yield; lp: Line pairs; NIR-II: Second near infrared; Xr-LEI: X-ray luminescence extension imaging; UC: Upconversion; PDMS: Polydimethylsiloxane; DS: Downshifting; LSO:Ce: Lu_2SiO_5:Ce; STE: Self-trapped exciton; XPDT: X-Ray effected photodynamic therapy; $Ba[Pt(CN)_4]$: Barium platino-cyanide; ROS: Reactive oxygen species; CaS: Calcium sulphide; CBM: Conduction band minimum.

Acknowledgements

This work was supported by the Zhejiang Provincial Natural Science Foundation of China (No. LZ21A040002), the National Natural Science Foundation of China (No. 52172164). The Institute for Lasers, Photonics and Biophotonics acknowledges support from the Office of Vice President for Research and Economic Development at the university at Buffalo.

Author contributions

Lei Lei and Yubin Wang contributed equally to this work. All authors read and approved the final manuscript.

Declarations

Competing interests

The authors declare that they have no competing interests.

Received: 3 August 2022 Revised: 3 August 2022 Accepted: 22 August 2022
Published online: 19 September 2022

References

1. H. Lusic, M.W. Grinstaff, X-ray-computed tomography contrast agents. Chem. Rev. **113**, 1641–1666 (2013)
2. G. Robb, Ultra-tunable graphene light source. Nat. Photon. **10**, 3–4 (2016)
3. X. Chen, J. Song, X. Chen, H. Yang, X-ray-activated nanosystems for theranostic applications. Chem. Soc. Rev. **48**, 3073–3101 (2019)
4. L. Lu, M. Sun, Q. Lu, T. Wu, B. Huang, High energy X-ray radiation sensitive scintillating materials for medical imaging, cancer diagnosis and therapy. Nano Energy **79**, 105437 (2021)
5. G. Blasse, Scintillator materials. Chem. Mater. **1994**(6), 1465–1475 (1994)
6. A. Kamkaew, F. Chen, Y. Zhan, R.L. Majewski, W. Cai, Scintillating nanoparticles as energy mediators for enhanced photodynamic therapy. ACS Nano **10**, 3918–3935 (2016)
7. Z. Wang et al., Non-invasive classification of microcalcifications with phase-contrast X-ray mammography. Nat. Commun. **5**, 3797 (2014)
8. G. Wang et al., A deep-learning pipeline for the diagnosis and discrimination of viral, non-viral and COVID-19 pneumonia from chest X-ray images. Nat. Biomed. Eng. **5**, 509–521 (2021)
9. A. Momose, T. Takeda, Y. Itai, K. Hirano, Phase-contrast X-ray computed tomography for observing biological soft tissues. Nat. Med. **2**, 473–475 (1996)
10. O. Rabin, J.M. Perez, J. Grimm, G. Wojtkiewicz, R. Weissleder, An X-ray computed tomography imaging agent based on long-circulating bismuth sulphide nanoparticles. Nat. Mater. **5**, 118–122 (2006)
11. L.-J. Xu, X. Lin, Q. He, M. Worku, B. Ma, Highly efficient eco-friendly X-ray scintillators based on an organic manganese halide. Nat. Commun. **11**, 4329 (2020)
12. P. Li et al., 4th generation synchrotron source boosts crystalline imaging at the nanoscale. Light Sci. Appl. **11**, 73 (2022)
13. R. Chen, P. Liu, T. Xiao, L.X. Xu, X-ray imaging for non-destructive microstructure analysis at SSRF. Adv. Mater. **26**, 7688–7691 (2014)
14. M. Holler et al., High-resolution non-destructive three-dimensional imaging of integrated circuits. Nature **543**, 402–406 (2017)
15. H. Wei et al., Sensitive X-ray detectors made of methylammonium lead tribromide perovskite single crystals. Nat. Photon. **10**, 333–339 (2016)
16. S. Akcay, T. Breckon, Towards automatic threat detection: a survey of advances of deep learning within X-ray security imaging. Pattern Recogn. **122**, 108245 (2022)
17. Y.G. Zdesenko et al., Scintillation properties and radioactive contamination of $CaWO_4$ crystal scintillators. Nucl. Instrum. Methods. Phys. Res. Sect. A. **538**, 657–667 (2005)
18. J.A. Shepherd, S.E. Sobottka, M.B. Williams, Performance and fabrication of thin film NaI(Tl) scintillators for use on imaging photomultiplier tubes. IEEE Trans. Nucl. Sci. **40**, 413–416 (1993)
19. I.G. Valais et al., Luminescence properties of (Lu, $Y_)2Si_O5$: Ce and G_d2Si_O5: Ce single crystal scintillators. IEEE Trans. Nucl. Sci. **54**, 11–18 (2007)

20. B.D. Milbrath, A.J. Peurrung, M. Bliss, W.J. Weber, Radiation detector materials: an overview. J. Mater. Res. **23**, 2561–2581 (2008)
21. J.K. Chen, N. Shirahata, H.T. Sun, Metal-free scintillators excite X-ray community. Nat. Photon. **15**, 171–172 (2021)
22. Q. Chen et al., All-inorganic perovskite nanocrystal scintillators. Nature **561**, 88–93 (2018)
23. H. Chen et al., $LiGa_5O_8$:Cr-based theranostic nanoparticles for imaging-guided X-ray induced photodynamic therapy of deep-seated tumors. Mater. Horiz. **4**, 1092–1101 (2017)
24. D. Ding et al., X-ray-activated simultaneous near-infrared and short-wave infrared persistent luminescence imaging for long-term tracking of drug delivery. ACS Appl. Mater. Interfaces **13**, 16166–16172 (2021)
25. R. Yasuda, M. Kataigiri, M. Matsubayashi, Influence of powder particle size and scintillator layer thickness on the performance of Gd_2O_2S: Tb scintillators for neutron imaging. Nucl. Instrum. Methods. Phys. Res. Sect. A. **680**, 139–144 (2012)
26. W. Ma et al., Highly resolved and robust dynamic X-ray imaging using perovskite glass-ceramic scintillator with reduced light scattering. Adv. Sci. **8**, 2003728 (2021)
27. B. Yang et al., Lead-free halide Rb_2CuBr_3 as sensitive X-ray scintillator. Adv. Mater. **31**, 1904711 (2019)
28. L. Lian et al., Efficient and reabsorption-free radioluminescence in $Cs_3Cu_2I_5$ nanocrystals with self-trapped excitons. Adv. Sci. **7**, 2000195 (2020)
29. T. Jiang et al., Power conversion efficiency enhancement of low-band-gap mixed Pb-Sn perovskite solar cells by improved interfacial charge transfer. ACS Energy Lett. **4**, 1784–1790 (2019)
30. Y. Gao et al., Highly stable lead-free perovskite field-effect transistors incorporating linear π-conjugated organic ligands. J. Am. Chem. Soc. **141**, 15577–15585 (2019)
31. T. Jiang et al., Realizing high efficiency over 20% of low-bandgap Pb-Sn-alloyed perovskite solar cells by in situ reduction of Sn^{4+}. Sol. RRL **4**, 1900467 (2019)
32. D. Liu et al., Three-dimensional controlled growth of monodisperse sub-50 nm heterogeneous nanocrystals. Nat. Commun. **7**, 10254 (2016)
33. Q. Su et al., The effect of surface coating on energy migration-mediated upconversion. J. Am. Chem. Soc. **134**, 20849–20857 (2012)
34. Y. Fan et al., Lifetime-engineered NIR-II nanoparticles unlock multiplexed in vivo imaging. Nat. Nanotech. **13**, 941–946 (2018)
35. Y. Zhong et al., In vivo molecular imaging for immunotherapy using ultra-bright near-infrared-IIb rare-earth nanoparticles. Nat. Biotechnol. **37**, 1322–1331 (2019)
36. D.K. Chatterjee, A.J. Rufaihah, Y. Zhang, Upconversion fluorescence imaging of cells and small animals using lanthanide doped nanocrystals. Biomaterials **29**, 937–943 (2008)
37. J. Zhou, Z. Liu, F. Li, Upconversion nanophosphors for small-animal imaging. Chem. Soc. Rev. **41**, 1323–1349 (2012)
38. M. Tan et al., Rare-earth-doped fluoride nanoparticles with engineered long luminescence lifetime for time-gated in vivo optical imaging in the second biological window. Nanoscale **10**, 17771–17780 (2018)
39. F. Wang et al., Tuning upconversion through energy migration in core-shell nanoparticles. Nat. Mater. **10**, 968–973 (2011)
40. D. Wang et al., ICG-sensitized $NaYF_4$: Er nanostructure for theranostics. Adv. Opt. Mater. **6**, 1701142 (2018)
41. Y. Li, S. Zeng, J. Hao, Non-invasive optical guided tumor metastasis/vessel imaging by using lanthanide nanoprobe with enhanced down-shifting emission beyond 1500 nm. ACS Nano **13**, 248–259 (2019)
42. Z. Chen et al., Low dose of X-ray-excited long-lasting luminescent concave nanocubes in highly passive targeting deep-seated hepatic tumors. Adv. Mater. **31**, 1905087 (2019)
43. Y. Zhuang, L. Wang, Y. Lv, T. Zhou, R. Xie, Optical data storage and multicolor emission readout on flexible films using deep-trap persistent luminescence materials. Adv. Funct. Mater. **28**, 1705769 (2018)
44. X. Ou et al., High-resolution X-ray luminescence extension imaging. Nature **590**, 410–415 (2021)
45. P. Thibault, M. Dierolf, A. Menzel, O. Bunk, C. David, F. Pfeiffer, High-resolution scanning X-ray diffraction microscopy. Science **321**, 379–382 (2008)
46. M. Dierolf et al., Ptychographic X-ray computed tomography at the nanoscale. Nature **467**, 436–439 (2010)
47. W.C. Rontgen, On a new kind of rays. Nature **53**, 274–276 (1895)
48. M. Suga et al., Native structure of photosystem II at 1.95 Å resolution viewed by femtosecond X-ray pulses. Nature **517**, 99–103 (2015)
49. C. Leveille et al., Ultrafast time-evolution of chiral Neel magnetic domain walls probed by circular dichroism in x-ray resonant magnetic scattering. Nat. Commun. **13**, 1412 (2022)
50. S. Yakunin et al., Detection of X-ray photons by solution-processed lead halide perovskites. Nat. Photon. **9**, 444–449 (2015)
51. J. Zhao et al., Perovskite-filled membranes for flexible and large-area direct-conversion X-ray detector arrays. Nat. Photon. **14**, 612–617 (2020)
52. M. Spahn, X-ray detectors in medical imaging. Nucl. Instrum. Methods Phys. Res. Sect. A. **731**, 57–63 (2013)
53. C. D'Ambrosio, F. De Notaristefani, H. Leutz, D. Puertols, E. Rosso, X-ray detection with a scintillating YAP-window hybrid photomultiplier tube. IEEE Trans. Nucl. Sci. **47**, 6–12 (2000)
54. C. Carrier, R. Lecomte, Recent results in scintillation detection with silicon avalanche photodiodes. IEEE Trans. Nucl. Sci. **37**, 209–214 (1990)
55. H. Wei, J. Huang, Halide lead perovskites for ionizing radiation detection. Nat. Commun. **10**, 1066 (2019)
56. B.K. Cha et al., Investigation of the performance of scintillator-based CMOS flat panel detectors for X-ray and thermal neutron imaging. IEEE Trans. Nucl. Sci. **57**, 1409–1413 (2010)
57. F. Cao et al., Shining emitter in stable host: design halide perovskite scintillators for X-ray imaging from commercial concept. ACS Nano **14**, 5183–5193 (2020)
58. Z. Lin, S. Lv, Z. Yang, J. Qiu, S. Zhou, Structured scintillators for efficient radiation detection. Adv. Sci. **9**, 2102439 (2022)
59. J.B. Birks, Scintillations from organic crystals: specific fluorescence and relative response to different radiations. Proc. Phys. Soc. A **64**, 874 (1951)
60. F. Maddalena et al., Inorganic, organic, and perovskite halides with nanotechnology for high-light yield X- and γ-ray scintillators. Curr. Comput.-Aided Drug Des. **9**, 88 (2019)
61. M.J. Weber, Inorganic scintillators: today and tomorrow. J. Lumin. **100**, 35–45 (2002)
62. Y. Wang, X. Yin, J. Chen, Y. Wang, Z. Chai, S. Wang, Gleaming uranium: an emerging emitter for building X-ray scintillators. Chem.-Eur. J. **26**, 1900–1905 (2020)
63. A. Chaudhry, R. Boutchko, S. Chourou, G. Zhang, N. Gronbech-Jensen, A. Canning, First-principles study of luminescence in Eu^{2+}-doped inorganic scintillators. Phys. Rev. B **89**, 155105 (2014)
64. C. Dujardin et al., Needs, trends, and advances in inorganic scintillators. IEEE Trans. Nucl. Sci. **65**, 1977–1997 (2018)
65. T. Yanagida et al., Optical and scintillation properties of bulk ZnO crystal. Phys. Status Solidi C **9**, 2284–2287 (2012)
66. T. Yanagida, Y. Fujimoto, M. Koshimizu, Evaluation of scintillation properties of GaN. Surf. Sci. Nanotechnol. **12**, 396–399 (2014)
67. V.B. Mikhailik, H. Kraus, J. Imber, D. Wahl, Scintillation properties of pure CaF_2. Nucl. Instrum. Methods Phys. Res. A **566**, 522–525 (2006)
68. R.Y. Shendrik, A. Radzhabov, A.I. Nepomnyashchikh, Scintillation properties of SrF_2 and SrF_2-Ce^{3+} crystals. Tech. Phys. Lett. **39**, 587–590 (2013)
69. M. Laval et al., Barium fluoride-inorganic scintillator for subnanosecond timing. Nucl. Instrum. Meth. Phys. Res. **206**, 169–176 (1983)
70. T. Yanagida et al., Growth and scintillation properties of $BaMgF_4$. Nucl. Instrum. Methods Phys. Res. A **621**, 473–477 (2010)
71. M. Moszynski, R. Allemand, M.R. Odru, J. Vacher, Laval Recent progress in fast timing with CsF scintillators in application to time-of-flight positron tomography in medicine. Nucl. Instrum. Methods Phys. Res. Sect. A **205**, 239–249 (1983)
72. Y. Tokuda, K. Sakaguchi, T. Nishihara, K. Takano, T. Fukushima, M. Hangyo, X-ray detection capability of a Cs_2ZnCl_4 single- crystal scintillator. Appl. Phys. Exp. **7**, 062602–1–062602–4 (2014)
73. M.J. Weber, R.R. Monchamp, Luminescence of $Bi_4Ge_3O_{12}$: spectral and decay properties. J. Appl. Phys. **44**, 5495–5499 (1973)
74. D.F. Anderson, Properties of the high-density scintillator cerium fluoride. IEEE Trans. Nucl. Sci. **36**, 137–140 (1989)
75. E. Garcia-Torano, B. Caro, V. Peyres, M. Mejuto, Characterization of a $CeBr_3$ detector and application to the measurement of some materials from steelworks. Nucl. Instrum. Methods Phys. Res. A **837**, 63–68 (2016)
76. Y. Fujimoto et al., Thallium magnesium chloride: a high light yield, large effective atomic number, intrinsically activated crystalline scintillator

for X-ray and gamma-ray detection. Jpn. J. Appl. Phys. **55**, 090301–1–090301–3 (2016).
77. H. Masai, T. Yanagida, Y. Fujimoto, M. Koshimizu, T. Yoko, Scintillation property of rare earth-free SnO-doped oxide glass. Appl. Phys. Lett. **101**, 191906 (2012)
78. T. Kato, G. Okada, T. Yanagida, Optical, scintillation and dosimeter properties of MgO transparent ceramic doped with Mn^{2+}. J. Ceram. Soc. Jpn. **124**, 559–563 (2016)
79. T. Kato, G. Okada, T. Yanagida, Optical, scintillation and dosimeter properties of MgO translucent ceramic doped with Cr^{3+}. Opt. Mater. **54**, 134–138 (2016)
80. Y. Futami, T. Yanagida, Y. Fujimoto, Optical, dosimetric, and scintillation properties of pure sapphire crystals. Jpn. J. Appl. Phys. **53**, 02BC12 (2014)
81. T. Kato, G. Okada, T. Yanagida, Optical, scintillation and dosimeter properties of MgO transparent ceramic and single crystal. Ceram. Int. **42**, 5617–5622 (2016)
82. T.A. Edison, Communication to Lord Kelvin. Nature **53**, 470 (1896)
83. W. Crookes, The emanations of radium. Proc. R. Soc. Lond. **71**, 405–408 (1903)
84. E. Sakai, Recent measurements on scintillator-photodetector systems. IEEE Trans. Nucl. Sci. **34**, 418–422 (1987)
85. I. Holl, E. Lorenz, G. Mageras, A measurement of the light yield of common inorganic scintillators. IEEE Trans. Nucl. Sci. **35**, 105–109 (1988)
86. Y. Shimizu, M. Minowa, W. Suganuma, Y. Inoue, Dark matter search experiment with CaF_2(Eu) scintillator at Kamioka Observatory. Phys. Lett. B **633**, 195–200 (2006)
87. B.C. Grabmaier, Crystal scintillators. IEEE Trans. Nucl. Sci. **31**, 372–376 (1984)
88. T. Yanagida, Inorganic scintillating materials and scintillation detectors. Proc. Jpn. Acad. Ser. B **94**, 75–97 (2018)
89. M.J. Weber, R.R. Monchamp, Luminescence of $Bi_4Ge_3O_{12}$-spectral and decay properties. J. Appl. Phys. **44**, 5495–5499 (1973)
90. C.L. Melcher, J.S. Schweitzer, Cerium-doped lutetium oxyorthosilicate-a fast, efficient new scintillator. IEEE Trans. Nucl. Sci. **39**, 502–505 (1992)
91. L. Pidol et al., High efficiency of lutetium silicate scintillators, Ce-doped LPS, and LYSO crystals. IEEE Trans. Nucl. Sci. **51**, 1084–1087 (2004)
92. K. Kamada et al., Composition engineering in cerium-doped (Lu, $Gd_)3(Ga, A_l)_{5O}12$ single-crystal scintillators. Cryst. Growth Des. **11**, 4484–4490 (2011)
93. R.T. Williams, W.W. Wolszczak, X. Yan, D.L. Carroll, Perovskite quantum-dot-in-host for detection of ionizing radiation. ACS Nano **14**, 5161–5169 (2020)
94. R.-Y. Zhu, C.L. Woody, Inorganic scintillators. Phys. Lett. B **667**, 286 (2008)
95. H. Nakamura, H. Kitamura, R. Hazama, Development of a new rectangular NaI(Tl) scintillator and spectroscopy of low-energy charged particles. Rev. Sci. Instrum. **81**, 013104 (2010)
96. P. Schotanus, P. Dorenbos, C.W.E. van Eijk, H.F. Lamfers, Suppression of the slow scintillation light output of BaF_2 crystals by La^{3+} doping. Nucl. Instrum. Methods Phys. Res. A **281**, 162–166 (1989)
97. R. Shendrik, E. Radzhabov, Absolute light yield measurements on SrF_2 and BaF_2 doped with rare earth ions. IEEE Trans. Nucl. Sci. **61**, 406–410 (2014)
98. T. Seo, New method for the centroid-shift analysis of picosecond lifetime measurements using BaF_2 scintillators. Nucl. Instrum. Methods Phys. Res. A **325**, 176–186 (1993)
99. K. Takagi, T. Fukazawa, Cerium activated Gd_2SiO_5 single crystal scintillator. Appl. Phys. Lett. **42**, 43 (1983)
100. V.V. Avdeichikov et al., Light output and energy resolution of CsI, YAG, GSO, BGO and LSO scintillators for light ions. Nucl. Instrum. Methods Phys. Res. A **349**, 216–224 (1994)
101. Z. Ma, X. Bi, X. Liu, D. Li, J. Li, X. Sun, Preliminary exploration on the preparation of LYSO: Ce single crystal using verneuil method. Mater. Sci. Forum **1003**, 247–253 (2020)
102. J. Xu, L. Fan, Y. Shi, J. Li, J. Xie, F. Lei, Effects of Ce^{3+} doping concentrations on microstructure and luminescent properties of Ce^{3+}: $Lu_3Al_5O_{12}$ (Ce: LuAG) transparent ceramics. Opt. Mater. **36**, 1954–1958 (2014)
103. M. Nikl, Scintillation detectors for X-rays. Meas. Sci. Technol. **17**, R37–R54 (2006)
104. M.V.S. Rezende, P.J.R. Montes, A.B. Andrade, Z.S. Macedo, M.E.G. Valerio, Mechanism of X-ray excited optical luminescence (XEOL) in europium doped $BaAl_2O_4$ phosphor. Phys. Chem. Chem. Phys. **18**, 17646–17654 (2016)
105. S.J. Duclos et al., Development of the HiLightTM scintillator for computed tomography medical imaging. Nucl. Instrum. Methods Phys. Res. A **505**, 68–71 (2003)
106. G.B. Schober, J.N. Anker, Radioluminescence imaging of drug elution from biomedical implants. Adv. Funct. Mater. **32**, 2106508 (2022)
107. V. Kumar, Z. Luo, A review on x-ray excited emission decay dynamics in inorganic scintillator materials. Photonics **8**, 71 (2021)
108. J. Ma et al., Highly efficient $NaGdF_4$: Ce/Tb nanoscintillator with reduced afterglow and light scattering for high-resolution X-ray imaging. ACS Appl. Mater. Interfaces **13**, 44596–44603 (2021)
109. Y. Zhou, J. Chen, O.M. Bakr, O.F. Mohammed, Metal halide perovskites for X-ray imaging scintillators and detectors. ACS Energy Lett. **6**, 739–768 (2021)
110. J.-C.G. Bunzli, C. Piguet, Taking advantage of luminescent lanthanide ions. Chem. Soc. Rev. **34**, 1048–1077 (2005)
111. X. Zhu et al., Temperature-feedback upconversion nanocomposite for accurate photothermal therapy at facile temperature. Nat. Commun. **7**, 10437 (2016)
112. F. Ahmad et al., Codoping enhanced radioluminescence of nanoscintillators for X-ray-activated synergistic cancer therapy and prognosis using metabolomics. ACS Nano **13**, 10419–10433 (2019)
113. N.M. Idris, M.K. Gnanasammandhan, J. Zhang, P.C. Ho, R. Mahendran, Y. Zhang, In vivo photodynamic therapy using upconversion nanoparticles as remote-controlled nanotransducers. Nat. Med. **18**, 1580–1585 (2012)
114. J. Wang et al., Enhancing multiphoton upconversion through energy clustering at sublattice level. Nat. Mater. **13**, 157–162 (2013)
115. K. Lingeshwar Reddy, R. Balaji, A. Kumar, V. Krishnan, Lanthanide doped near infrared active upconversion nanophosphors: fundamental concepts, synthesis strategies, and technological applications. Small **14**, 1801304 (2018)
116. D.R. Cooper, J.A. Capobianco, J. Seuntjens, Radioluminescence studies of colloidal oleate-capped β-Na (Gd, $Lu)_f$4: L^{n3}+ nanoparticles (Ln= Ce, Eu, Tb). Nanoscale **10**, 7821–7832 (2018)
117. V. Yakovyna, Y. Zhydachevskii, V.B. Mikhailik, I. Solskiic, D. Sugakc, M. Vakivc, Effect of thermo-chemical treatments on the luminescence and scintillation properties of CaWO4. Opt. Mater. **30**, 1630–1634 (2008)
118. A.A. Demidenko et al., Scintillation parameters of BaF_2 and BaF_2: Ce^{3+} ceramics. Opt. Mater. **32**, 1291–1293 (2010)
119. X. Wang et al., Photo/cathodoluminescence and stability of Gd_2O_2S: Tb, Pr green phosphor hexagons calcined from layered hydroxide sulfate. J. Am. Ceram. Soc. **101**, 5477–5486 (2018)
120. M. Yoneyama et al., Evaluation of GAGG: Ce scintillators for future space applications. J. Instrum. **13**, P02023 (2018)
121. R. Ma, L. Zhang, R. Zhu, Optical and scintillation properties of inorganic scintillators in high energy physics. IEEE Trans. Nucl. Sci. **55**, 2425–2431 (2008)
122. X. Qin, X. Liu, W. Huang, M. Bettinelli, X. Liu, Lanthanide-activated phosphors based on 4f–5d optical transitions: theoretical and experimental aspects. Chem. Rev. **117**, 4488–4527 (2017)
123. W.M. Higgins, A. Churilov, E. van Loef, J. Glodo, M. Squillante, K. Shah, Crystal growth of large diameter $LaBr_3$: Ce and $CeBr_3$. J. Cryst. Growth **310**, 2085–2089 (2008)
124. C.L. Melcher, Scintillators for well logging applications. Nucl. Instrum. Methods Phys. Res. A **40**, 1214–1218 (1989)
125. E. Sysoeva, V. Tarasov, O. Zelenskaya, Comparison of the methods for determination of scintillation light yield. NNucl. Instrum. Methods Phys. Res. A **486**, 67–73 (2002)
126. M. Nikl, A. Yoshikawa, Recent R&D trends in inorganic single-crystal scintillator materials for radiation detection. Adv. Opt. Mater. **3**, 463–481 (2015)
127. F. Zhou, Z. Li, W. Lan, Q. Wang, L. Ding, Z. Jin, Halide perovskite, a potential scintillator for X-Ray detection. Small Methods **4**, 2000506 (2020)
128. W. Huda, R.B. Abrahams, X-ray-based medical imaging and resolution. Am. J. Roentgenol. **204**, W393–W397 (2015)
129. J. Zhou et al., Impact of lanthanide nanomaterials on photonic devices and smart applications. Small **14**, 1801882 (2018)

130. L. Lei et al., Amplifying upconversion by engineering interfacial density of state in sub-10 nm colloidal core/shell fluoride nanoparticles. Nano Lett. **24**, 10222–10229 (2021)
131. F. Wang, R. Deng, X. Liu, Preparation of core-shell $NaGdF_4$ nanoparticles doped with luminescent lanthanide ions to be used as upconversion-based probes. Nat. Protoc. **9**, 1634–1644 (2014)
132. G. Chen et al., Core/shell $NaGdF_4$:Nd^{3+}/$NaGdF_4$ nanocrystals with efficient near-infrared to near-infrared downconversion photoluminescence for bioimaging applications. ACS Nano **6**, 2969–2977 (2012)
133. L. Song et al., Low-dose X-ray activation of W(VI)-doped persistent luminescence nanoparticles for deep-tissue photodynamic therapy. Adv. Funct. Mater. **28**, 1707496 (2018)
134. W. Xu, L. Lei, Y. Wang, E. Liu, L. Chen, S. Xu, Modulating electron population pathways for time-dependent dynamic multicolour displays. Mater. Horiz. **8**, 3443–3448 (2021)
135. W. Fan et al., Breaking the depth dependence by nanotechnology-enhanced X-ray-excited deep cancer theranostics. Adv. Mater. **31**, 1806381 (2019)
136. F. Wang, X. Liu, Multicolor tuning of lanthanide-doped nanoparticles by single wavelength excitation. Accounts Chem. Res. **47**, 1378–1385 (2014)
137. Y. Wu, W. Wu, Combinations of superior inorganic phosphors for level-tunable information hiding and encoding. Adv. Opt. Mater. **9**, 2100281 (2021)
138. B. Liu, C. Li, P. Yang, Z. Hou, J. Lin, 808-nm-Light-excited lanthanide-doped nanoparticles: rational design, luminescence control and theranostic applications. Adv. Mater. **29**, 1605434 (2017)
139. G. Gao et al., Up-conversion fluorescent labels for plastic recycling: a review. Adv. Sustain. Syst. **1**, 1600033 (2017)
140. P.M. Kraus, M. Zurch, S.K. Cushing, D.M. Neumark, S.R. Leone, The ultrafast X-ray spectroscopic revolution in chemical dynamics. Nat. Rev. Chem. **2**, 82–94 (2018)
141. E.F. Garman, Developments in x-ray crystallographic structure determination of biological macromolecules. Science **343**, 1102–1108 (2014)
142. C.M. Jeffries et al., Small-angle X-ray and neutron scattering. Nat. Rev. Methods Primers **1**, 70 (2021)
143. J. Scharf et al., Bridging nano- and microscale X-ray tomography for battery research by leveraging artificial intelligence. Nat. Nanotechnol. (2022). https://doi.org/10.1038/s41565-022-01081-9
144. A. Einstein, Uber einen Erzeugung und Verwandlung des lichtes betreffenden heuristischen Gesichtspunkt. Ann. Phys. **17**, 132–148 (1905)
145. A.H. Compton, A quantum theory of the scattering of X-rays by light elements. Phys. Rev. **21**, 483 (1923)
146. J.J. Thomson, On electrical oscillations and the effects produced by the motion of an electrified sphere. Proc. Lond. Math. Soc. **1**, 197–219 (1883)
147. G. Matt, M. Feroci, M. Rapisarda, E. Costa, Treatment of Compton scattering of linearly polarized photons in Monte Carlo codes. Radiat. Phys. Chem. **48**, 403–411 (1996)
148. M. Rizzi, M. D'Aloia, B. Castagnolo, Semiconductor detectors and principles of radiation-matter interaction. J. Appl. Sci. **10**, 3141–3155 (2010)
149. H.J. Ache, Chemistry of the positron and of positronium. Angew. Chem. Int. Edit. **11**, 179–199 (1972)
150. T. Enoto et al., Photonuclear reactions triggered by lightning discharge. Nature **551**, 481–484 (2017)
151. L. Li et al., Mechanism of the trivalent lanthanides' persistent luminescence in wide bandgap materials. Light Sci. Appl. **11**, 1–8 (2022)
152. X. Zhong et al., $NaCeF_4$: Gd, Tb scintillator as an X-ray responsive photosensitizer for multimodal imaging-guided synchronous radio/radiodynamic therapy. Nano Lett. **19**, 8234–8244 (2019)
153. Y. Zhuang et al., X-ray-charged bright persistent luminescence in $NaYF_4$: Ln^{3+}@ NaYF4 nanoparticles for multidimensional optical information storage. Light Sci. Appl. **10**, 1–10 (2021)
154. T. Passuello et al., Structural and optical properties of Vernier phase lutetium oxyfluorides doped with lanthanide ions: interesting candidates as scintillators and X-ray phosphors. J. Mater. Chem. **22**, 10639–10649 (2012)
155. P. Dorenbos, Relation between Eu^{2+} and Ce^{3+} f↔d-transition energies in inorganic compounds. J. Phys. Condens. Matter **15**, 4797–4807 (2003)
156. G. Li, Y. Tian, Y. Zhao, J. Lin, Recent progress in luminescence tuning of Ce^{3+} and Eu^{2+}-activated phosphors for pc-WLEDs. Chem. Soc. Rev. **44**, 8688–8713 (2015)
157. L. Lei et al., Modulation of surface energy transfer cascade for reversible photoluminescence pH sensing. Chem. Mater. **31**, 8121–8128 (2019)
158. J. Liu et al., Simultaneously excited downshifting/upconversion luminescence from lanthanide-doped core/shell fluoride nanoparticles for multimode anticounterfeiting. Adv. Funct. Mater. **28**, 1707365 (2018)
159. H. Huang et al., Lanthanide-doped core@ multishell nanoarchitectures: multimodal excitable upconverting/downshifting luminescence and high-level anti-counterfeiting. Small **16**, 2000708 (2020)
160. Z. Qiu, S. Wang, W. Wang, S. Wu, Polymer composites entrapped Ce-doped $LiYF_4$ microcrystals for high-sensitivity X-ray scintillation and omaging. ACS Appl. Mater. Interfaces **12**, 29835–29843 (2020)
161. Y.-M. Yang et al., X-ray-activated long persistent phosphors featuring strong UVC afterglow emissions. Light Sci. Appl. **7**, 1–11 (2018)
162. K. Fukuda, T. Yanagida, Y. Fujimoto, N. Kawaguchi, H. Sekiya, Study of vacuum ultraviolet scintillation in rare earth doped Lutetium fluoride. 2013 IEEE NSS/MIC 1–3 (2013).
163. J. Pejchal et al., Crystal growth and scintillation properties of selected fluoride crystals for VUV scintillators. J. Cryst. Growth **401**, 833–838 (2014)
164. O.L. Malta, L.D. Carlos, Intensities of 4f–4f transitions in glass materials. Quim. Nova **26**, 889–895 (2003)
165. K. Li, X. Liu, Y. Zhang, X. Li, H. Lian, J. Lin, Host-sensitized luminescence properties in $CaNb_2O_6$: Ln^{3+} (Ln^{3+}= Eu^{3+}/Tb^{3+}/Dy^{3+}/Sm^{3+}) phosphors with abundant colors. Inorg. Chem. **54**, 323–333 (2015)
166. C.L. Hsu, S.J. Chang, Doped ZnO 1D nanostructures: synthesis, properties, and photodetector application. Small **10**, 4562–4585 (2014)
167. S. Zhang et al., Highly sensitive InSb nanosheets infrared photodetector passivated by ferroelectric polymer. Adv. Funct. Mater. **30**, 2006156 (2020)
168. L. Tu, X. Liu, F. Wu, H. Zhang, Excitation energy migration dynamics in upconversion nanomaterials. Chem. Soc. Rev. **44**, 1331–1345 (2015)
169. R. Deng, F. Qin, R. Chen, M. Hong, X. Liu, Temporal full-colour tuning through non-steady-state upconversion. Nat. Nanotech. **10**, 237–242 (2015)
170. X. Xu et al., Optimising passivation shell thickness of single upconversion nanoparticles using a time-resolved spectrometer. APL Photon. **4**, 026104 (2019)
171. L. Liu, F. Qin, H. Zhao, T. Lv, Z. Zhang, W. Cao, Shell thickness dependence of upconversion luminescence of β-$NaYF_4$: Yb, Er/β-$NaYF_4$ core-shell nanocrystals. Opt. Lett. **38**, 2101–2103 (2013)
172. L.G. Jacobsohn et al., Synthesis, luminescence and scintillation of rare earth doped lanthanum fluoride nanoparticles. Opt. Mater. **33**, 136–140 (2010)
173. P. Pei et al., X-ray-activated persistent luminescence nanomaterials for NIR-II imaging. Nat. Nanotechnol. **16**, 1011–1018 (2021)
174. C. Li et al., In vivo real-time visualization of tissue blood flow and angiogenesis using Ag_2S quantum dots in the NIR-II window. Biomaterials **35**, 393–400 (2014)
175. G. Hong et al., Ultrafast fluorescence imaging in vivo with conjugated polymer fluorophores in the second near-infrared window. Nat. Commun. **5**, 4206 (2014)
176. J. Yan, B. Li, P. Yang, J. Lin, Y. Dai, Progress in light-responsive lanthanide nanoparticles toward deep tumor theranostics. Adv. Funct. Mater. **31**, 2104325 (2021)
177. Y. Liu et al., Significantly enhanced afterglow brightness via intramolecular energy transfer. ACS Materials Lett. **3**, 713–720 (2021)
178. Y. Li, M. Gecevicius, J. Qiu, Long persistent phosphors-from fundamentals to applications. Chem. Soc. Rev. **45**, 2090–2136 (2016)
179. H. Singh, S.K. Bhardwaj, M. Khatri, K.-H. Kim, N. Bhardwaja, UVC radiation for food safety: an emerging technology for the microbial disinfection of food products. Chem. Eng. J. **417**, 128084 (2021)
180. K. Huang et al., Three-dimensional colloidal controlled growth of core-shell heterostructured persistent luminescence nanocrystals. Nano Lett. **21**, 4903–4910 (2021)

181. Y. Wang et al., $NaMgF_3:Tb^{3+}@NaMgF_3$ nanoparticles containing deep traps for optical information storage. Adv. Opt. Mater. **9**, 2100624 (2021)
182. Z. Li, H. Li, H. Sun, X-ray-activated UVA long persistent luminescence from defective fluoride elpasolites. J. Rare Earths **38**, 124–129 (2020)
183. Y. Hu et al., X-ray-excited super-long green persistent luminescence from Tb^{3+} monodoped β-$NaYF_4$. J. Phys. Chem. C **124**, 24940–24948 (2020)
184. G. Chen, C. Yang, P.N. Prasad, Nanophotonics and nanochemistry: Controlling the excitation dynamics for frequency up- and down-conversion in lanthanide-doped nanoparticles. Accounts Chem. Res. **46**, 1474–1486 (2013)
185. K. Sankaranarayanan, J.S. Wassom, Reflections on the impact of advances in the assessment of genetic risks of exposure to ionizing radiation on international radiation protection recommendations between the mid-1950s and the present. Mutation Res. **658**, 1–27 (2008)
186. K. Masaoka, T. Yamashita, Y. Nishida, M. Sugawara, Modified slanted-edge method and multidirectional modulation transfer function estimation. Opt. Express **22**, 6040–6046 (2014)
187. F. Viallefont-Robinet et al., Comparison of MTF measurements using edge method: towards reference data set. Opt. Express **26**, 33625–33648 (2018)
188. H. Lu, X. Xu, G. Feng, B. Sun, S. Wang, S. Wu, Terbium doped $LiLuF_4$ nanocrystal scintillator-based flexible composite film for high resolution X-ray imaging. RSC Adv. **12**, 4615–4623 (2022)
189. S. Clement, W. Deng, E. Camilleri, B.C. Wilson, E.M. Goldys, X-ray induced singlet oxygen generation by nanoparticle-photosensitizer conjugates for photodynamic therapy: Determination of singlet oxygen quantum yield. Sci. Rep. **6**, 19954 (2016)
190. T. Rimoldi et al., CeF_3-ZnO scintillating nanocomposite for self-lighted photodynamic therapy of cancer. J. Mater. Sci. Mater. Med **27**, 159 (2016)
191. D.R. Cooper, K. Kudinov, P. Tyagi, C.K. Hill, S.E. Bradforth, J.L. Nadeau, Photoluminescence of cerium fluoride and cerium-doped lanthanum fluoride nanoparticles and investigation of energy transfer to photosensitizer molecules. Phys. Chem. Chem. Phys. **16**, 12441–12453 (2014)
192. M.Y. Losytskyy, L.V. Kuzmenko, O.B. Shcherbakov, N.F. Gamaleia, A.I. Marynin, V.M. Yashchuk, Energy transfer in $Ce_{0.85}Tb_{0.15}F_3$ nanoparticles-CTAB shell-Chlorin e6 system. Nanoscale Res. Lett. **12**, 294 (2017)
193. Y. Tang, J. Hu, A. Elmenoufy, X. Yang, Highly efficient FRET system capable of deep photodynamic therapy established on X-ray excited mesoporous LaF_3: Tb scintillating nanoparticles. ACS Appl. Mater. Interfaces **7**, 12261–12269 (2015)
194. M. Jiang, Z. Xue, Y. Li, H. Liu, S. Zeng, J. Hao, A soft X-ray activated lanthanide scintillator for controllable NO release and gas-sensitized cancer therapy. Nanoscale Horiz. **5**, 268–273 (2020)
195. J. Zhou, X. Zhu, M. Chen, Y. Sun, F. Li, Water-stable NaLuF4-based upconversion nanophosphors with long-term validity for multimodal lymphatic imaging. Biomaterials **33**, 6201–6210 (2012)
196. Y. Liu, K. Ai, J. Liu, Q. Yuan, Y. He, L. Lu, A high-performance ytterbium-based nanoparticulate contrast agent for in vivo X-ray computed tomography imaging. Angew. Chem. Int. Ed. **124**, 1466–1471 (2012)
197. L. Xu et al., Construction of high quality ultrathin lanthanide oxyiodide nanosheets for enhanced CT imaging and anticancer drug delivery to efficient cancer theranostics. Biomaterials **230**, 119670 (2020)
198. C. Ronda, H. Wieczorek, V. Khanin, P. Rodnyi, Review-Scintillators for medical imaging: a tutorial overview. ECS J. Sol. State Sci. Technol. **5**, 3121–3125 (2016)
199. Y. Dai et al., Mussel-inspired polydopamine-coated lanthanide nanoparticles for NIR-II/CT dual imaging and photothermal therapy. ACS Appl. Mater. Interfaces **9**, 26674–26683 (2017)
200. T. Jia et al., Mesoporous cerium oxide-coated upconversion nanoparticles for tumor-responsive chemo-photodynamic therapy and bioimaging. Chem. Sci. **10**, 8618–8633 (2019)
201. Y. Song et al., Energy migration control of multimodal emissions in an Er^{3+}-doped nanostructure for information encryption and deep-learning decoding. Angew. Chem. Int. Edit. **133**, 23983–23989 (2021)
202. Y. Xie, Y. Song, G. Sun, P. Hu, A. Bednarkiewicz, L. Sun, Lanthanide-doped heterostructured nanocomposites toward advanced optical anti-counterfeiting and information storage. Light Sci. Appl. **11**, 1–10 (2022)
203. Y. Khan et al., A flexible organic reflectance oximeter array. Proc. Natl. Acad. Sci. USA **115**, E11015–E11024 (2018)
204. H. Xu, J. Liu, J. Zhang, G. Zhou, N. Luo, N. Zhao, Flexible organic/inorganic hybrid near-infrared photoplethysmogram sensor for cardiovascular monitoring. Adv. Mater. **29**, 1700975 (2017)
205. A. El Gamal, H. Eltoukhy, CMOS image sensors. IEEE Circuits Devices Mag. **21**, 6–20 (2005)
206. Y. Song et al., Digital cameras with designs inspired by the arthropod eye. Nature **497**, 95–99 (2013)
207. T. Mueller, F. Xia, P. Avouris, Graphene photodetectors for high-speed optical communications. Nat. Photon. **4**, 297–301 (2010)
208. C. Bao et al., High performance and stable all-inorganic metal halide perovskite-based photodetectors for optical communication applications. Adv. Mater. **30**, 1803422 (2018)
209. M. Boberl, M.V. Kovalenko, S. Gamerith, E.J.W. List, W. Heiss, Inkjet-printed nanocrystal photodetectors operating up to 3 μm wavelengths. Adv. Mater. **19**, 3574–3578 (2007)
210. J. Chen et al., A submicrosecond-response ultraviolet-visible-near-infrared broadband photodetector based on 2D tellurosilicate $inSiTe_3$. ACS Nano (2022). https://doi.org/10.1021/acsnano.1c11628
211. J. Michel, J. Liu, L. Kimerling, High-performance Ge-on-Si photodetectors. Nat. Photon. **4**, 527–534 (2010)
212. L. Xie et al., Broadband detection of X-ray, ultraviolet, and near-infrared photons using solution-processed perovskite-lanthanide nanotransducers. Adv. Mater. **33**, 2101852 (2021)
213. G. Anjaiah, S.K.N. Rasool, P. Kistaiah, Spectroscopic and visible luminescence properties of rare earth ions in lead fluoroborate glasses. J. Lumin. **159**, 110–118 (2015)
214. Y. Wang et al., Integrating positive and negative thermal quenching effect for ultrasensitive ratiometric temperature sensing and anti-counterfeiting. ACS Appl. Mater. Interfaces **13**, 23951–23959 (2021)
215. J. Legendziewicz, M. Guzik, J. Cybinska, VUV spectroscopy of double phosphates doped with rare earth ions. Opt. Mater. **31**, 567–574 (2009)
216. Y. Liu, J. Zhang, C. Zhang, J. Jiang, H. Jiang, High efficiency green phosphor $Ba_9Lu_2Si_6O_{24}:Tb^{3+}$: visible quantum cutting via cross-relaxation energy transfers. J. Phys. Chem. C **120**, 2362–2370 (2016)
217. X. Ou et al., Recent development in X-ray imaging technology: future and challenges. Research **2021**, 9892152 (2021)